

**LA-9748-MS**

*c. 3*

CIC-14 REPORT COLLECTION

**REPRODUCTION  
COPY**

Los Alamos National Laboratory is operated by the University of California for the United States Department of Energy under contract W-7405-ENG-36.

*The Los Alamos Laser Simulation of  
High-Altitude Nuclear Explosion Effects:  
Final Report*



**Los Alamos** Los Alamos National Laboratory  
Los Alamos, New Mexico 87545

This work was supported by the Defense Nuclear Agency

Edited by Glenda Ponder and Marge Wilson, ESS Division

**DISCLAIMER**

This report was prepared as an account of work sponsored by an agency of the United States Government. Neither the United States Government nor any agency thereof, nor any of their employees, makes any warranty, express or implied, or assumes any legal liability or responsibility for the accuracy, completeness, or usefulness of any information, apparatus, product, or process disclosed, or represents that its use would not infringe privately owned rights. Reference herein to any specific commercial product, process, or service by trade name, trademark, manufacturer, or otherwise, does not necessarily constitute or imply its endorsement, recommendation, or favoring by the United States Government or any agency thereof. The views and opinions of authors expressed herein do not necessarily state or reflect those of the United States Government or any agency thereof.

LA-9748-MS

UC-34

Issued: September 1983

**The Los Alamos Laser Simulation of  
High-Altitude Nuclear Explosion Effects:  
Final Report**



T. H. Tan  
A. H. Williams  
J. E. Borovsky  
M. B. Pongratz



**Los Alamos** Los Alamos National Laboratory  
Los Alamos, New Mexico 87545

• •  
• •

• •

## CONTENTS

ABSTRACT	1
I.    MOTIVATION FOR THE EXPERIMENT	1
II.   THE EXPERIMENT	4
III.  EXPERIMENTAL RESULTS	6
A.  Laser-Target Coupling	6
B.  Ion Generation	6
C.  Ion Velocity Distributions	13
D.  Ion Interaction with Background Gas	14
E.  Modification of Ion Acceleration	17
IV.  MODELING THE RESULTS	19
A.  Background Air Plasma	19
B.  Debris Ions	23
C.  Collisional Effects on the Expansion	25
D.  Collisional Effects on Air Plasma	27
V.   COMPARISON WITH OTHER LASER EXPERIMENTS	30
VI.  CONCLUSIONS AND RECOMMENDATIONS	31
A.  Conclusions	31
B.  Recommendations	33
ACKNOWLEDGMENTS	35
APPENDIX A.  SCALING RELATIONS	37
APPENDIX B.  DETECTORS	41
APPENDIX C.  ESTIMATES OF AIR PLASMA PARAMETERS	44
APPENDIX D.  COLLISIONAL EFFECTS	49
REFERENCES	61

THE LOS ALAMOS LASER SIMULATION OF  
HIGH-ALTITUDE NUCLEAR EXPLOSION EFFECTS:  
FINAL REPORT

by

T. H. Tan, A. H. Williams, J. E. Borovsky, and M. B. Pongratz

ABSTRACT

The early time effects of high-altitude nuclear explosions have been experimentally simulated by irradiating spherical targets with eight beams from the Helios CO<sub>2</sub> laser in a chamber containing air at various pressures. The following experimental conditions have been established by various studies to closely match the requirements for proper simulation: (1) the laser-target ion expansion velocity can be adjusted to equal the weapon debris velocity; (2) background gas is pre-ionized; (3) sufficient debris-ion kinetic energy is available; and (4) the explosions are spherically symmetric. In the absence of a background magnetic field, strong coupling between the kinetic energy of the target ions and the background air plasma was not observed. The capabilities and limitations for high-altitude nuclear explosion simulations with high-power CO<sub>2</sub> lasers are now better understood.

---

I. MOTIVATION FOR THE EXPERIMENT

The detonation of a nuclear weapon produces a large quantity of energetic plasma debris. At low altitudes, this debris interacts with the ambient atmosphere through classical collisions; at sufficiently high altitudes, the mean free paths for these collisions are enormous and additional physics must

be invoked to explain the observed coupling between debris and the ambient ionosphere.

Longmire<sup>1</sup> proposed that the ionized debris cloud begins its interaction with the atmosphere by coupling into the earth's magnetic field, sweeping up both the field and the ionized background. This mechanism yields a debris-ion coupling length of the order of an ion gyroradius. The available weapons data are consistent with this mechanism.

However, the relative streaming of the debris and air ions may give rise to ion-ion plasma instabilities that may appreciably shorten the coupling distance and significantly affect the rates of cross-field diffusion and pitch-angle scattering for both ion species.

A prototype simulation experiment has been carried out at the Los Alamos Helios laser facility to study whether such "collisionless" coupling may contribute to the early time dynamics of high-altitude nuclear explosions (HANE). Laser simulations offer rapid reproducibility and a capability for varying parameters (including the collisionality), which are advantages even over real events. Further, in situ diagnostics can reveal the first-principle physics of the debris-air coupling.

Laser simulations of high-altitude events may be classified as global or limited. Global simulations attempt to reproduce most, if not all, features of a weapon burst. Limited simulations are geared to specific physical problems.

Criteria for the global simulation of HANE have been outlined in several studies.<sup>2-4</sup> The Los Alamos experiment has been guided by the following.

- (1) Preservation of the debris-ion velocity. This ensures that collisional and ionization cross sections, very sensitive functions of velocity, are preserved.
- (2) Pre-ionization of ambient air. Collisionless coupling manifests itself in collective interactions between the debris plasma and the ambient air plasma.
- (3) Spherical symmetry of the explosion. Asymmetric expansions are susceptible to polarization-charge effects that may dominate their motions.
- (4) Sufficient debris-ion energy. This is critical for scaling to the high-altitude explosions of interest.

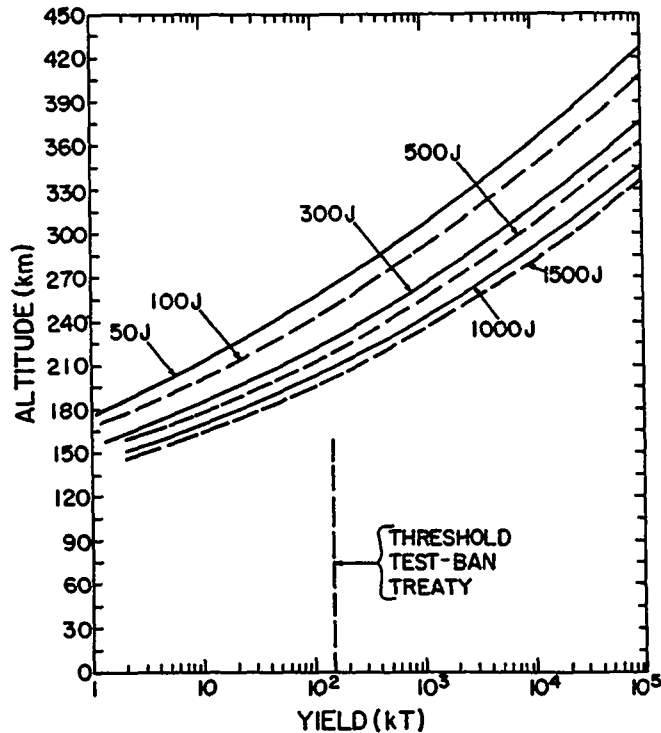


Fig. 1. The scaling of a laser experiment. Each curve gives the scaled HANE yield obtainable if the laser experiment produces the stated energy of target ions when there is 0.1 torr of air in the target chamber. The CIRA Model-5 (hour = 22) atmosphere<sup>5</sup> was used to transform the air density into altitude. The Helios experiment follows the 300-J curve.

Scaling a laboratory simulation to a high-altitude explosion has been outlined by Longmire et al.<sup>3</sup> (see also Appendix A). Figure 1 depicts the altitude-yield curves scaled from a laser experiment with a given kinetic energy of fast ions and with 0.1 torr of fully ionized air in the chamber to a weapon burst in a model atmosphere.<sup>5</sup> The Helios experiment, with 300 J of ions with the preserved velocities at 0.1-torr chamber air pressure, is the basis for simulating a weapon with a total yield of 1 Mt at altitudes of 240 km or higher.

Although the primary objective is to simulate early time HANE events by investigating fast-ion coupling to background plasmas in the laboratory, the other goals of this first kilojoule-range laser experiment are to verify that the conditions required for useful simulation could be properly met by the Helios laser system.

## II. THE EXPERIMENT

Experimental simulations of the HANE early time effects have been performed in the Helios CO<sub>2</sub> laser facility<sup>6</sup> at the Los Alamos National Laboratory. In the Helios target chamber a spherical pellet is irradiated by eight beams of 10.6- $\mu$ m wavelength laser light, a total of up to 6100 J of energy being delivered in less than 1 ns. This laser light is coupled to the target by heating target electrons to a very high temperature, greater than 100 keV. The outward expansion of the hot electrons generates huge potentials, which subsequently accelerate target ions to very high velocities. The amount of energy transfer by such collisionless processes to the fast ions can represent as much as 70% of the total CO<sub>2</sub> laser energy absorbed by the target.

The air surrounding a HANE is simulated by air at pressures ranging from 10<sup>-6</sup> to 10 torr within the target chamber (1 torr = 1-mm Hg). Hot electrons from the high-Z target, through thermal and bremsstrahlung processes, emit approximately 10% of the absorbed laser energy in about 100-eV blackbody radiation (ultraviolet and x ray), which ionizes the air. At pressures of 1 torr and above, air breakdown occurs and the laser light is partially absorbed before reaching the target. This results in a lower limit to the scaled altitudes obtainable in the experiment. At lower pressures, a further limitation derives from the effect of the ambient air on the acceleration mechanism at the target.

Ion emission depends on the laser irradiance on the target surface. By varying the pellet diameter, the effective laser intensity is modified and the velocity distribution and the total kinetic energy of the debris ions can be controlled. By illuminating spherical targets (gold-coated 1- and 2-mm-diam glass microballoon, CH-coated 400- $\mu$ m-diam glass microballoon, and tungsten-coated nickel solacel) in vacuum ( $<1 \times 10^{-5}$ -torr air pressure), the total emitted ion kinetic energy can increase from 22% of the incident laser energy to above 50%. The fast-ion energy fraction (measured ion energy/incident laser energy), as defined by those ions penetrating a 0.5- $\mu$ m-thick nickel foil, can be increased from a mere 3% of the incident laser energy for a 2-mm-diam target to 28% for a 300- $\mu$ m-diam target (see Fig. 2). With 5000 J of incident laser energy, more than 660 J of very fast ion kinetic energy is available for high-velocity simulation with a 1-mm-diam target. With smaller targets, as much as 1750 J of total ion kinetic energy is available over a broader velocity range.

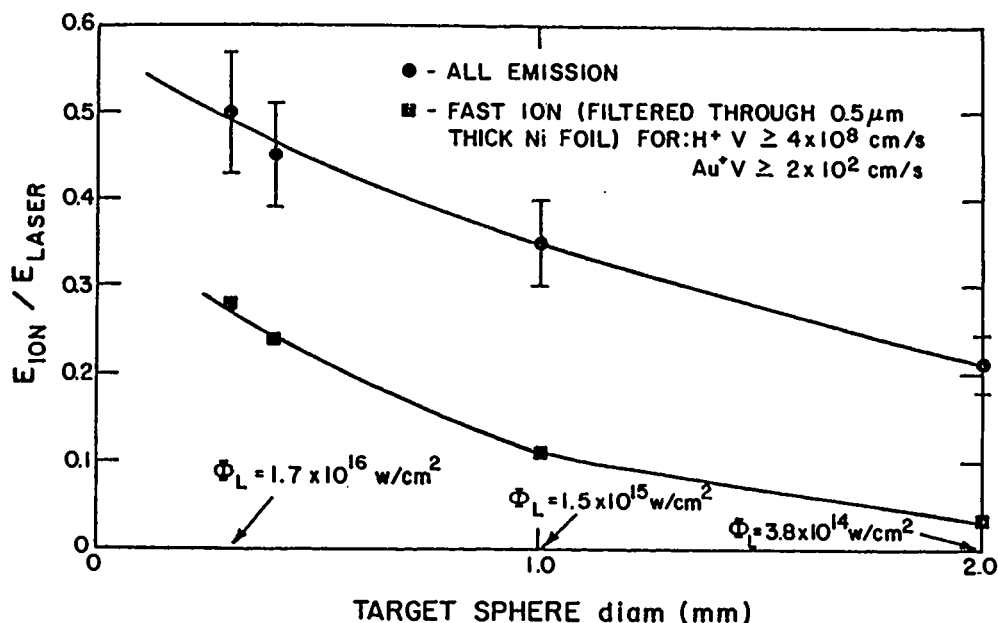


Fig. 2. The total ion kinetic energy emitted into vacuum from spherical targets at four different irradiances (target diameters). The measurements show that the amount of kinetic energy in the desired velocity range (as determined by open and 0.5- $\mu\text{m}$  nickel foil-filtered calorimeters) can be controlled.

Extensive x-ray, ion, and optical diagnostics were employed to ensure correct understanding of the physical processes involved and to determine if proper simulation conditions for Fish Bowl's events were satisfied as the background gas was introduced. These detectors are described in Appendix B.

Forty laser shots were fired with eight beams delivering 5 to 6 kJ on target in 0.7 ns (full width at half maximum) for the simulation. The illumination was such that the explosions were spherically symmetric. Another 25 shots were fired with 4- to 8-beam illumination on flat disks to determine the effects of the background gas on the ion acceleration. About three-fourths of the spherical target shots were fired with backfilled air and one-fourth with argon. The pressure varied from  $10^{-6}$  to 5 torr, most of the shots being between 0.1 and 1 torr. Spherical targets of various sizes (300- $\mu\text{m}$ , 1-mm, and 2-mm diam) were illuminated. In this first high-energy experiment most targets have a thin high-Z (tungsten, gold) coating to ensure that hard x-ray bremsstrahlung spectrum can be properly measured and that laser-target coupling can be unambiguously determined.

### III. EXPERIMENTAL RESULTS

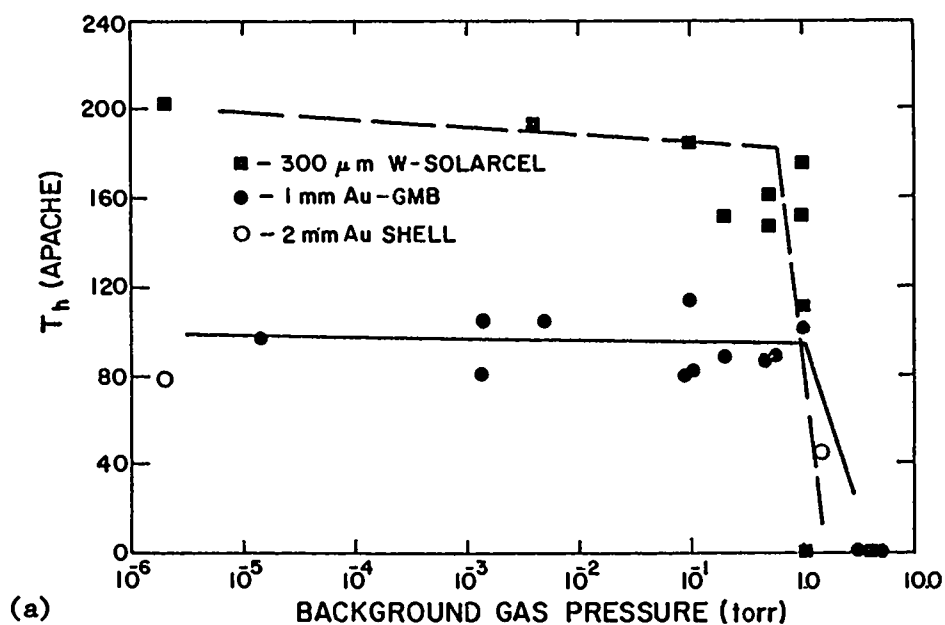
#### A. Laser-Target Coupling

Laser-target interaction appears not to be seriously affected by the presence of up to 1 torr of background air pressure. Laser energy coupling to the target is characterized by the target hot-electron energy distribution, which is manifested in the bremsstrahlung emission. The measured hard x-ray spectra (characterized by the hot-electron temperature  $T_h$ ) deduced from the slope of the energy distribution is plotted in Fig. 3a. The x-ray yield, which reflects the total energy content in the distribution, is shown in Fig. 3b. Preservation of  $T_h$  and the x-ray yield up to about 1 torr strongly suggests that the laser can be focused without dielectric breakdown even at an intensity level of  $\sim 1.7 \times 10^{16}$  W/cm<sup>2</sup>. Both the measured hot x-ray temperature and the measured hot x-ray yield drop rapidly as the background air pressure is raised above 1 torr. Beyond 1 torr the number and mean energy of the hot electrons are reduced and consequently less energy is absorbed by the target.

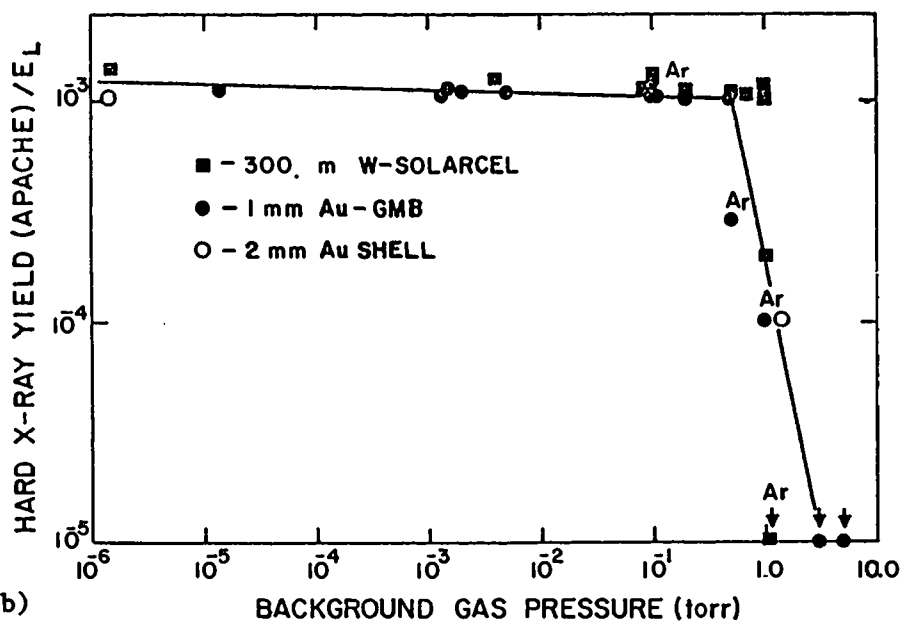
#### B. Ion Generation

1. Measurement at 175 cm from target. The total emitted ion kinetic energy and filtered fast-ion energy were measured by open and 0.5- $\mu$ m-thick nickel foil-filtered calorimeters at 175 cm from the target as a function of background air pressure. Data from 300- $\mu$ m-diam tungsten-coated nickel solacels and 1-mm-diam gold-coated glass microballoons, which correspond to laser target irradiances of  $1.7 \times 10^{16}$  W/cm<sup>2</sup> and  $1.5 \times 10^{15}$  W/cm<sup>2</sup>, are plotted, respectively, in Figs. 4a and 4b. At high irradiance over 50% of the incident laser energy can be converted into ion kinetic energy in a vacuum ( $< 10^{-5}$  torr). The filtered fast-ion energy represents typically between one-third and two-thirds of the total available ion kinetic energy. The threshold calorimeters allowed through only particles with speeds in excess of  $4.3 \times 10^8$  cm/s for protons,  $3.5 \times 10^8$  cm/s for carbon, and  $1.5 \times 10^8$  cm/s for gold.

The fraction of the ion kinetic energy appears to drop greatly as the background gas pressure increases. The solid curves in Fig. 4 are drawn merely to illustrate the trend. The decrease in slower ion energy may be partially accounted for by collisional loss. For fast ions, however, the decrease cannot be explained by collisional loss. We will show that a change in the ion acceleration mechanism arising from target electron leakage into the background gas is largely responsible. Another factor in the decrease is attributed to



(a)



(b)

Fig. 3. (a) The target hot-electron distributions (parameterized by the temperature  $T_h$ ) arising from laser interactions with 300- $\mu$ m-, 1-mm-, and 2-mm-diam tungsten- and gold-coated spherical targets as functions of the background air pressure. The solid lines are drawn arbitrarily to aid in viewing. (b) The measured hard x-ray yield from hot-electron bremsstrahlung plotted as a function of the background air pressure.

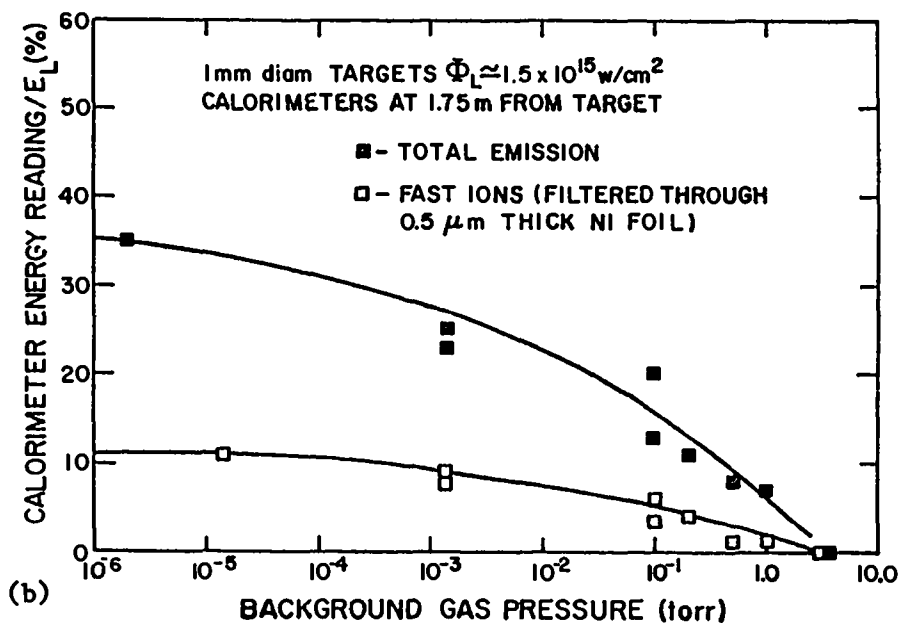
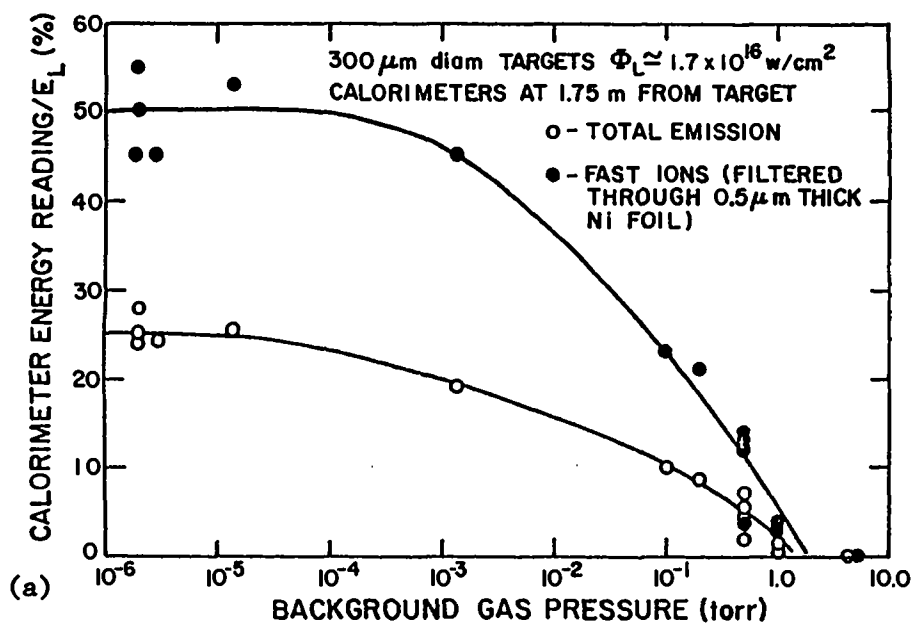


Fig. 4. (a) The total ion kinetic energy and the faster ion portion of the total, represented as fractions of the incident laser energy, as measured by open and 0.5- $\mu\text{m}$  nickel foil-filtered calorimeters located 175 cm from the 300- $\mu\text{m}$ -diam tungsten-coated solajel targets, plotted as functions of the background air pressure. (b) The same measurements as part (a) but with 1-mm-diam gold-coated targets. All solid curves are drawn arbitrarily to aid in viewing the experimental behavior.

the target ultraviolet and soft x-ray emissions that attenuate while ionizing the background air before reaching the calorimeters.

In these measurements several of the calorimeters were positioned to measure the angular distribution of both the total ion energy and the filtered fast-ion energy. They indicate spherical symmetry to within a factor of 2 over the entire  $4\pi$  steradians.

2. Measurement near the target. If either collisional loss or collisionless ion-air coupling processes significantly decrease the measured ion energy at 175 cm from the target, the same measurements at closer distance should show a smaller decrease. Total ion energy measurements were done with higher capacity open (unthresholded) calorimeters of 2.9 and 5.3 cm from the target; the results are shown in Fig. 5a. The data at 5.3 cm are normalized to those at 2.9 cm by the appropriate ratio of solid angles subtended by the detectors. The measurements were carried out at high laser irradiance ( $\sim 3 \times 10^{16}$  W/cm<sup>2</sup>). The data show a reduction with increasing background air pressure similar to measurements at 175 cm from the target, which is represented by the solid curve.

The use of thin nickel foil for thresholded energy measurement is not possible at close distance because it is readily punctured by the pressure wave from the laser-irradiated target. A different scheme was developed to measure the emitted fast-ion number. Here, a CD<sub>2</sub> target was irradiated and the emitted deuterons then impinged on a CD<sub>2</sub> foil placed only 1 cm away. The subsequent characteristic 2.45-MeV neutrons produced from the fusion reactions  $D+D \rightarrow H_e^3 + n$  were then detected by high time-resolved plastic scintillator-photomultiplier detectors and verified by a time-of-flight technique. Because the D-D reaction cross sections heavily favor fast deuterons, the measurement is primarily that of the faster ion component. To enhance measurement statistics, a double parallel flat foil target was employed. The results are plotted in Fig. 5b. Here the number of deuteron ions emitted from the laser target appears to decrease with increasing background air pressure, and the pattern is consistent with the filtered fast-ion measurements at 175 cm as represented by the solid curve. The preservation of ion velocity spectra at different background pressures is observed in charge-cup measurements; therefore, the velocity dependence of the neutron production cross section is not part of the interpretation.

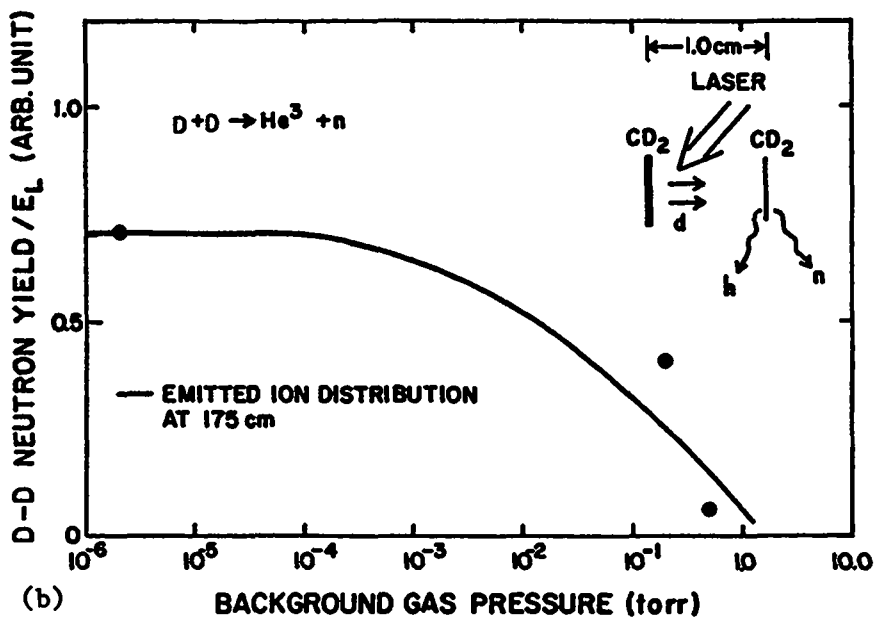
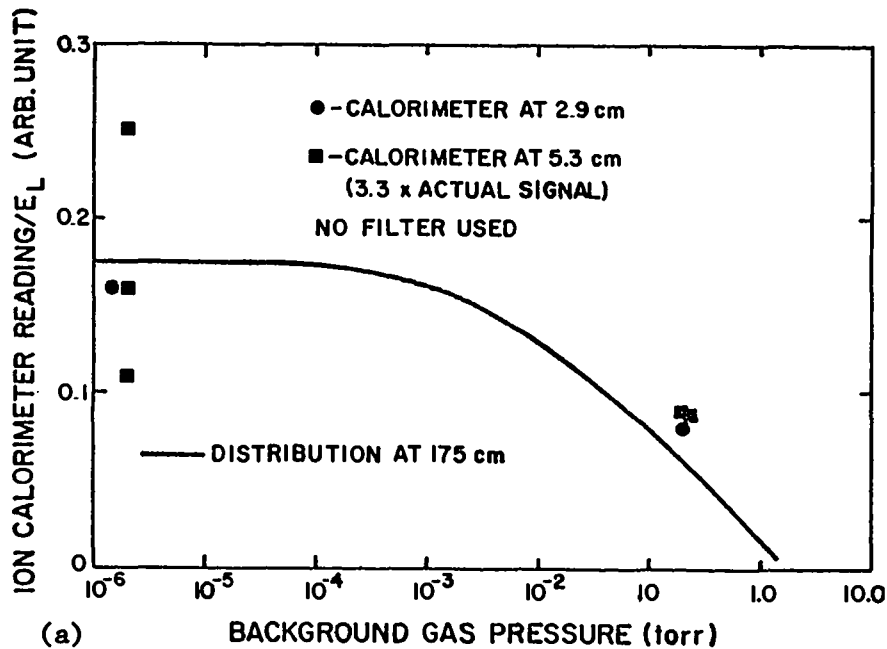


Fig. 5. (a) The total ion kinetic energy emitted from flat targets as measured by large open calorimeters located 2.9 and 5.3 cm from the targets for selected background air pressures. The solid curve represents the experimental distribution from measurements made at 175 cm from the target. (b) The fast deuteron ion emission from targets as determined from the neutron yield from D-D fusion reactions plotted as a function of the background air pressure. The solid curve represents the fast-ion kinetic energy fraction as determined by filtered calorimeters located 175 cm from the target.

The observed decrease in ion emission near the target with increasing background pressure strongly implies a significant modification in ion acceleration, which is due to the presence of air. Furthermore, the lack of evidence for collisional energy loss (as is implied by the constant ratio of total ion energy observed between the close-up measurements and measurements at 175 cm from the target), even when the background air pressure was increased to above 0.1 torr, strongly suggests that even those ions that do not penetrate the 0.5- $\mu\text{m}$ -thick nickel foil must have velocities very near  $10^8$  cm/s. Hence, the available kinetic energy of fast ions in the velocity range of interest ( $1\text{--}5 \times 10^8$  cm/s) should be in excess of the difference between the two curves on both Figs. 4a and 4b. The implication is that even with the ion-emission modification by the background gas, a significant amount of fast-ion kinetic energy is still available at 0.1 torr for HANE simulations in the Helios facility. More than 11% of the laser energy or at least 600 J at 6-kJ laser energy is still available when the irradiance is  $1.5 \times 10^{15}$  W/cm<sup>2</sup> or higher (see Fig. 6).

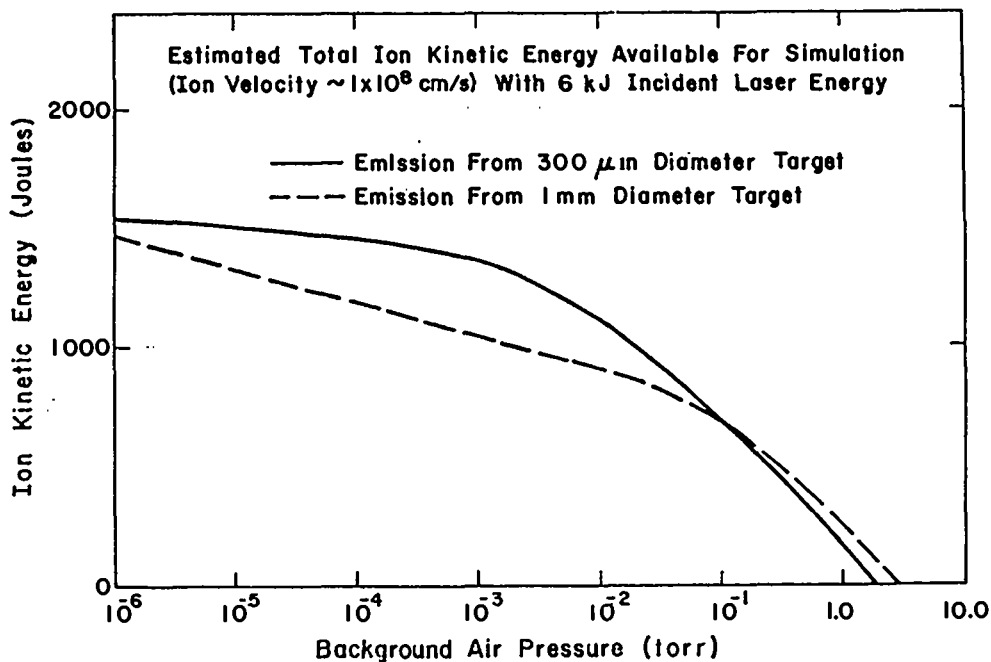
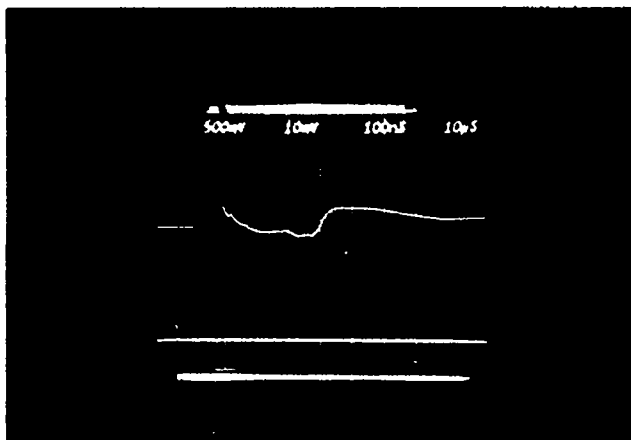


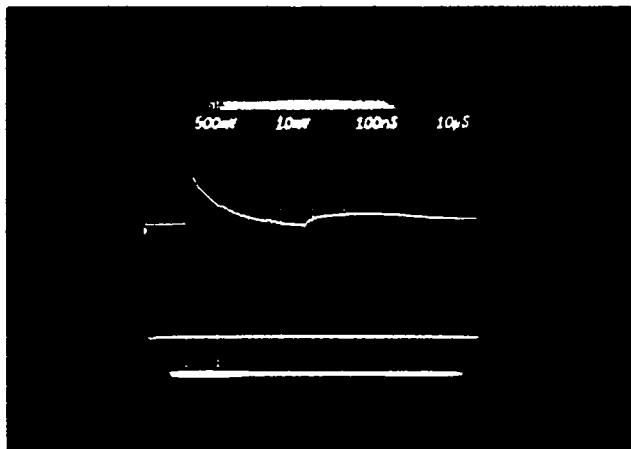
Fig. 6. Estimates of the available ion kinetic energy suitable for the simulation obtained from 300- $\mu\text{m}$ - and 1-mm-diam targets.

ION CURRENT DECREASES WITH INCREASING GAS  
PRESSURE, BUT THE SPECTRUM IS UNCHANGED

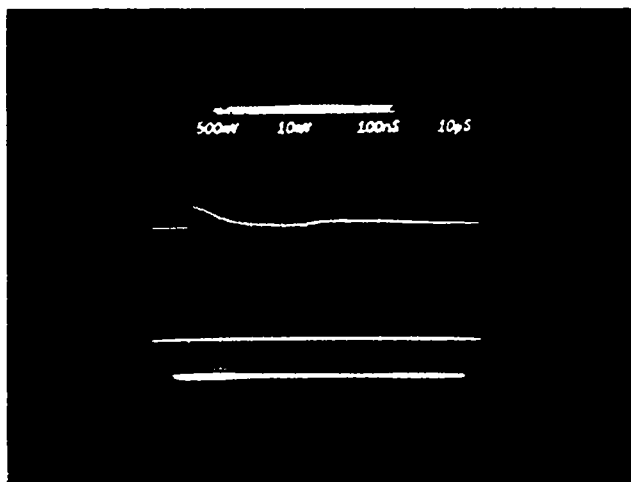
$$(V_{\text{IONS}} \leq 5.2 \times 10^8 \text{ cm/s})$$



$$P = 1.5 \times 10^{-3} \text{ TORR}$$



$$P = 9.5 \times 10^{-2} \text{ TORR}$$



$$P = 5 \times 10^{-1} \text{ TORR}$$

Fig. 7. Ion current measurements detected by charge cups located 175 cm from targets for three different background air pressures.

### C. Ion Velocity Distributions

Charge cups measure the time history of ions (current) arriving at 175 cm from the target. Figure 7 shows the charge-cup signals from 1-mm-diam gold-coated glass microballoon targets for three chamber pressures. The spectrum at  $<10^{-5}$  torr is the same as the one at  $10^{-3}$  torr and is not presented. The initial peak in the current profile results from a combination of the photon response of the charge cup and the very fast ions (target surface contaminant protons with speeds  $\sim 10^9$  cm/s). The presence of the very fast ions is independently determined by time-of-flight plastic scintillator-photomultiplier crab-eye detector measurements (see Appendix B). Thresholded calorimeter observations show  $\sim 500$  J in the fast-ion fraction for a 1-mm target in vacuum. Therefore, these very fast ions have no more than 500 J of kinetic energy. Such very fast ions may be present in an actual HANE. Special techniques have been developed to prevent ion generation, if necessary, by boiling off the hydrogen and carbon contaminants from the target surface before the laser shot.

The major component of the ion current is the signal beginning at  $\sim 400$  ns. The distance from the target being 175 cm, these ions are traveling at  $\sim 4.4 \times 10^8$  cm/s. By assuming that all the particles were accelerated simultaneously from a point source 175 cm from the cup and that they reach the detector without any interaction, the relative velocity distribution can be deduced. This  $dQ/dV$  spectrum is shown in Fig. 8. Note that the oscilloscope sweep setting precluded determining the velocity distribution for speeds  $< 2 \times 10^8$  cm/s. The observable portion of the velocity spectrum appears to be preserved as the background pressure increases, whereas the magnitude appears to decrease in the ratio consistent with the energy measurements discussed in Sec. III-B. This preservation of the velocity spectrum with increasing background air pressure can be expected because the collisional energy loss should not be significant. Because there has been no evidence of such signal in the charge cup when similar laser shots on plastic-coated glass microballoons were taken, these ions appear also to be gold ions. Without knowing the exact charge states of the gold ions, it is not possible to obtain the energy content in the observed spectrum. Based on the fact that those ions with velocities below the threshold of 0.5- $\mu$ m nickel foil do not seem to suffer significant collisional loss during the passage through 175 cm of 0.1-torr air (100% ionized nitrogen) and assuming an average charge state for gold of  $\sim 10$ , it can be estimated that the minimum velocity must be  $\sim 1 \times 10^8$  cm/s. Hence,

the bulk of the emitted ion velocity distribution lies in the velocity range of 1 to  $5 \times 10^8$  cm/s, falling exactly in the desired region for more straightforward HANE simulations.

D. Ion Interaction With Background Gas

Optical diagnostics were employed to directly observe the interaction of target-emitted ions with the background air and to investigate the background plasma conditions. The optical diagnostics consisted of: (a) time-resolved measurements of the visible emissions within a conical field of view, (b) time-integrated, spatially resolved camera images of the visible emissions, and (c) time-integrated spectra of the visible emissions. The spectrographic measurements indicate that the dominant emissions are molecular band emissions from neutral and ionized air. Some strong lines are also present in the data. The spectral resolution of the spectrograph is broader than any expected Doppler shifts, hence the observation of air motion is ruled out.

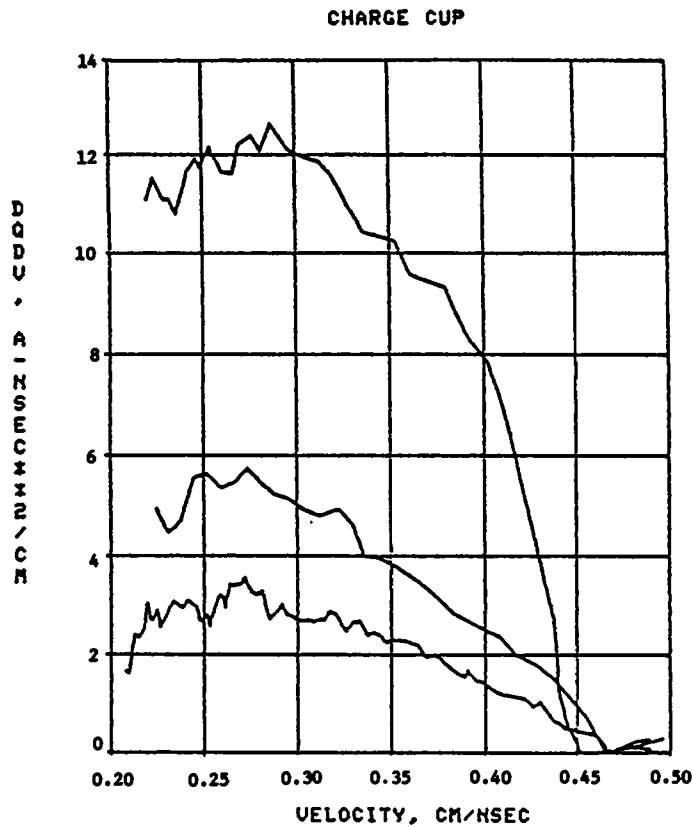


Fig. 8. Reconstructed charge-cup distributions as a function of velocity from the current measurements of Fig. 7.

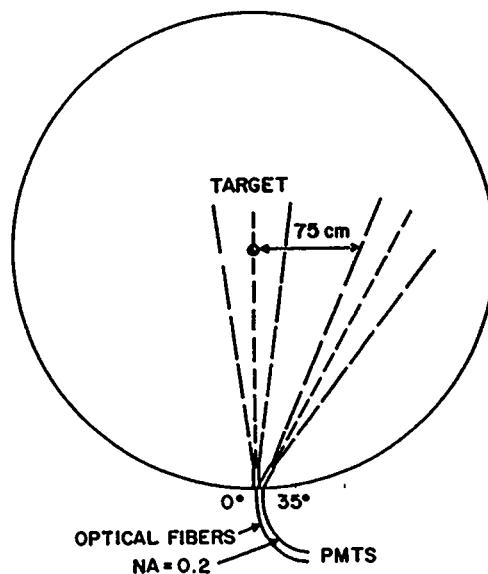


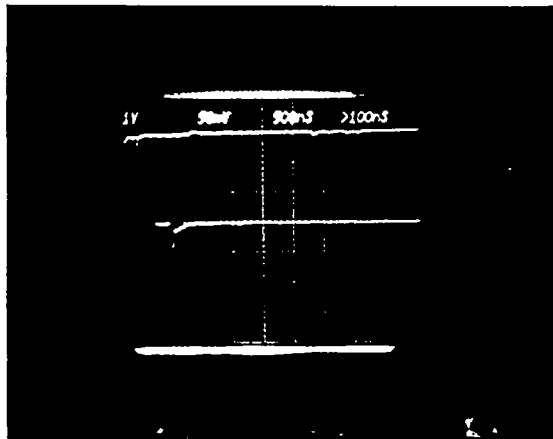
Fig. 9. A schematic drawing of the fiber-optic arrangement used for measuring the visible emission from target ion interactions with the background gas.

The time-resolved measurements show emission at locations and times that strongly imply interaction between "fast" target ions and background air. Figure 9 depicts the fiber-optic arrangement used to detect visible emission. Figure 10 displays representative data at different air pressures and target conditions. Two oscilloscope traces are displayed for each picture. The top trace records the output from the fiber directly viewing the target and the second trace records the signal from the (off-target) fiber viewing  $35^\circ$  away. The time-scale settings vary.

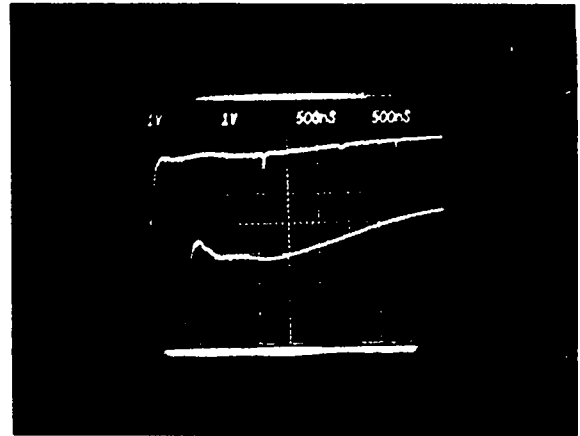
In vacuum, only light emitted from the target is observed, the off-target channel simply sees wall reflection. As the pressure is increased to  $5 \times 10^{-3}$  torr, a broad pulse with a long decay time of  $\sim 100$  ns is observed. This pulse can be explained by the excitation of air molecules by the x rays and ultraviolet radiation emitted from the target. It confirms the pre-ionization needed to satisfy the simulation criterion.

At  $2 \times 10^{-1}$  torr, significant ion-air interaction is observed regularly at around  $2 \times 10^8$  cm/s by the off-target fiber. Computer modeling of the temporal response of the off-target channel indicates that this signal is consistent with optical emissions from a thin shell expanding radially at  $\sim 2 \times 10^8$  cm/s. This is consistent with the velocity measured by charge cups and strongly

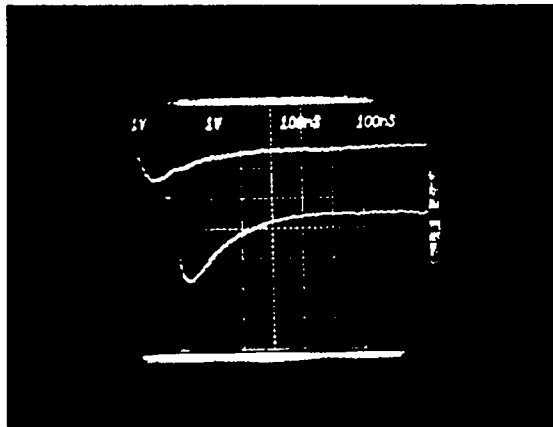
LIGHT EMISSION INDICATES ION-BACKGROUND GAS INTERACTIONS



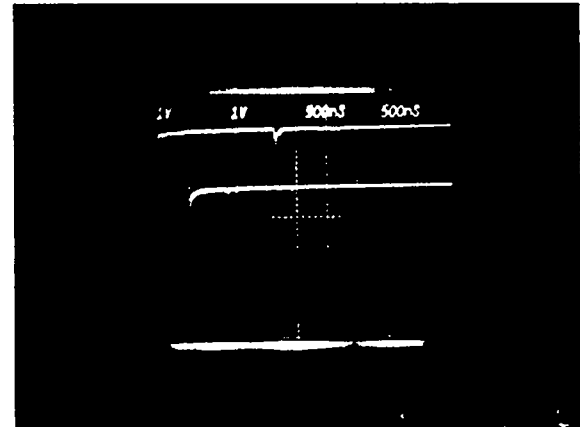
$P = 1.5 \times 10^{-6}$  TORR



$P = 2 \times 10^{-1}$  TORR



$P = 5 \times 10^{-3}$  TORR



$P = 2 \times 10^{-1}$  TORR (NO TARGET)

Fig. 10. Time-resolved visible emissions detected by optical fiber array as recorded on dual-trace oscilloscopes for laser shots at various background air pressures. The upper and lower traces represent the  $0^\circ$  and  $35^\circ$  viewing angles respectively. Note that no visible emission is recorded for laser shots without targets.

confirms a narrow velocity band that contains most of the ion kinetic energy observed.

The observed increase in light emission as a function of air pressure is consistent with the collisional excitation processes. No additional anomalous coupling mechanism is required to explain the data.

#### E. Modification of Ion Acceleration

Hot-electron leakage from the expanding target plasma into the background gas is evidenced by the drop in measured target potential (Fig. 11) as the background pressure increases. The resulting effect in modifying the ion acceleration is illustrated in Fig. 12 where the velocity of the expanding ion front, represented by the measured fastest ion velocity, is truncated. The target potential was measured with a voltage divider and an ultrafast 3-GHz oscilloscope was used to record the rapid flow of the returned current from the ground. The drop in measured returned current from the ground through the voltage-sampling divider circuit implies that the electrons leaving the target were rapidly replaced by electrons from the ambient ionized gas to preserved charge neutrality. The energetic electrons remaining in the expanding sheath

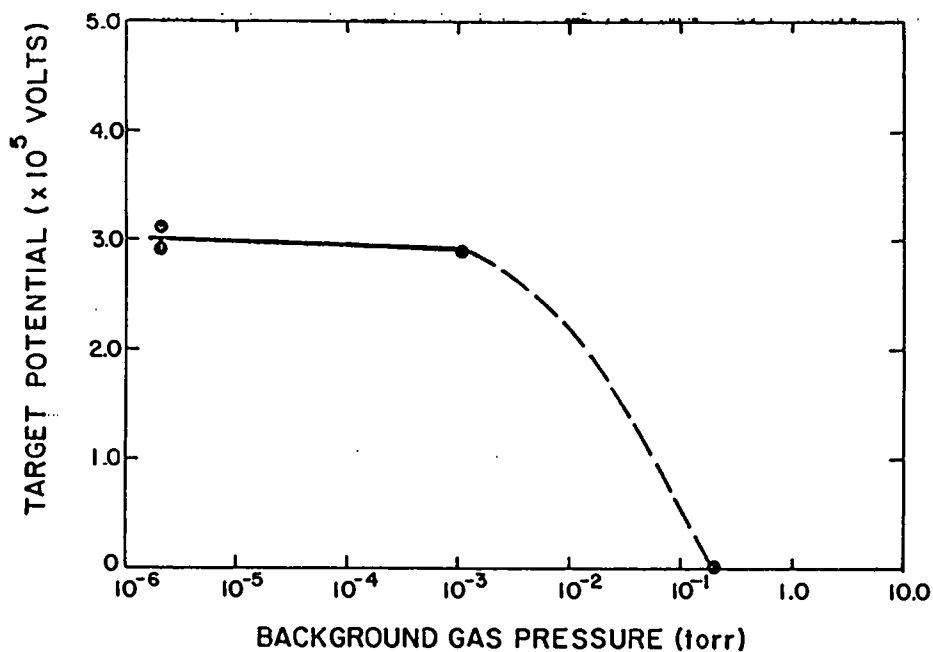


Fig. 11. The electrical potentials of the laser targets as determined by return current measurement are plotted against the background air pressure. The solid curve represents the experimental trend.

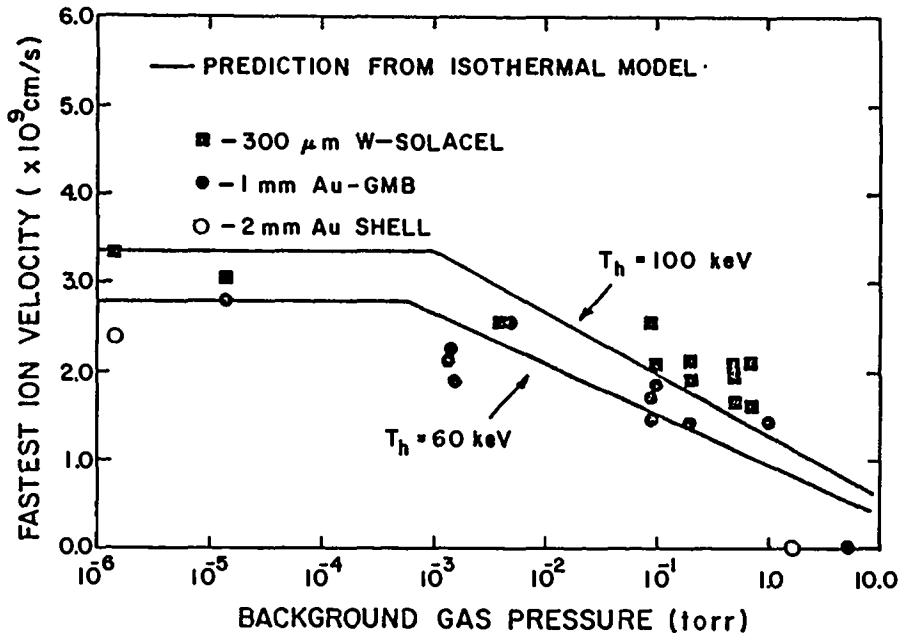


Fig. 12. The velocity of the fastest ion (as measured by the crab-eye detector) is plotted as a function of background air pressure. The solid lines represent calculations from an isothermal expansion model using two different ion-determined hot-electron temperatures corresponding to the two sets of data, one from 300- $\mu$ m- and one from 1-mm-diam targets.

were the ones that accelerated the bulk of the fast ions from the target. With ionized background gas near the target, these energetic "bound" electrons can readily interchange with the electrons in the gas and thus significantly reduce the potential that accelerates the ions. This could affect ion emission in two ways: slowing down the expanding ion front and reducing the total number of ions emitted. The effect on the fastest ion front expansion can be modeled by using an isothermal expansion model,<sup>7</sup> as do the solid curves in Fig. 12 representing two different sets of data corresponding to two different laser-irradiance conduit ions. In this model, the electron density can be derived from a Debye length that corresponds closely to the plasma expansion scale length  $c_s t$  (ion-sound-speed  $\times$  time). Typically, the number density of the expanding plasma front is between  $10^{12}$ - $10^{13}$  per  $\text{cm}^3$ , which corresponds to the background pressure of  $\sim 10^{-3}$  torr. When this underdense plasma expands into a colder, denser background medium, the background electrons can readily replace the hot electrons. This results in the immediate stoppage of ion acceleration in the vicinity of the expanding plasma front as is manifested in the truncation of the observed fast-ion velocity. In Fig. 12, it is evident that

this velocity truncation will not affect those expanding ions below  $1 \times 10^9$  cm/s, corresponding to a higher density, even at 1-torr pressure. This is consistent with the observed preservation of the ion velocity spectrum in Fig. 8.

Once the background electrons begin to diffuse into the expanding plasma sheath, the number of energetic electrons that accelerate the ions is reduced and this results in the observed overall reduction of ion emission (independent of velocity) as the background gas pressure increases.

One of the proposed mechanisms for explaining early time HANE phenomenon could also be contributing to the observed reduction in the number of ions when background gas is present. If sufficient amounts of ambient ions are present within the domain of laser-plasma scale length (a few mm from the target) and if these ions are under the influence of the target self-generated megagauss magnetic fields,<sup>8</sup> then the conditions may be conducive to strongly magnetized ion-ion streaming instabilities. The available coupling length may be short enough that some fraction of the ions are able to leave the region and be observed at 175 cm away without a slowing down of the peak velocity of  $\sim 5 \times 10^8$  cm/s, as in Fig. 8. Significant increase in the spherical glow in visible emissions around the target has been observed by the still camera when the air pressure is increased from  $10^{-5}$  torr to  $2 \times 10^{-1}$  torr (by comparing the corresponding target images in Figs. 13a and 13b). The glow spot is so intense that the recorded image on film is too saturated for densitometry analysis. This observation is consistent with possible magnetized ion-ion coupling very near the laser interaction surface; however, it does not constitute an experimental proof because many other complicating plasma processes are simultaneously at work here. The real investigation of magnetized ion-ion coupling must be, and can be, readily studied at some distance away from the CO<sub>2</sub> laser target.

#### IV. MODELING THE RESULTS

##### A. Background Air Plasma

Modeling of the background air plasma in the target chamber, necessary for the collisional calculations below, is described in this section. This air plasma arises from two sources, electromagnetic radiation from the hot target pellet and ionizing collisions with the outflowing target debris. Ionization by radiation is discussed first.



(a)



(b)

Fig. 13. Time-integrated photographs of the targets and surroundings from shots at (a)  $10^{-6}$ -torr and (b) 0.2-torr background air pressures.

Simple energy arguments indicate that target radiation is insufficient to fully ionize all of the air within the target chamber at the background pressures of interest. Typically 150 J of 100-eV blackbody radiation is emitted by the pellet, and Eq. (C-1) indicates that this 150 J of radiation deposited into 0.1 torr of air could produce a 100% ionized ( $F = 1$ ) sphere 14 cm in radius or a 1% ionized ( $F = 0.01$ ) sphere 65 cm in radius.

As is outlined in Appendix C, using the opacity to the peak blackbody photon for the 100-eV radiation yields energy deposition estimates [Eq. (C-3)] that lead to fractional ionization estimates [Eq. (C-4)] and electron temperature estimates [Eq. (C-5)], all as functions of the radius from the laser target. Estimated electron densities and electron temperatures of the air plasmas created by target radiation appear in Fig. 14. Most of the 150 J of target radiation is absorbed by the chamber walls, even for 1 torr of air. This is corroborated by the camera data of Table I showing little energy in air fluorescence. Thus, with little attenuation of the radiation from absorption by air, the extinction factor in Eq. (C-3) is nearly unity and the energy deposition, and hence the ionization number density, falls off approximately as  $r^{-2}$  from the target.

The ionization that arises from collisions between the debris particles and the air particles is harder to estimate. The chief source of collisional energy transfer comes through Coulomb collisions between the debris ions, which contain nearly all of the available energy, and the air electrons. These Coulomb interactions lead to a heating of the air electrons that indirectly produces ionization, a sensible estimate of which would be difficult to obtain. The ionization arising from inelastic atomic collisions between the debris ions and air atoms is much simpler to treat. After the method of Appendix C, Fig. 15 contains the ionization number density produced as a 300-J Maxwellian distribution of gold ions released from the target streams outward into 0.1 torr of air, along with a comparison with the number density of ionization produced by the 150 J of 100-eV radiation from the hot target. This figure indicates that the amount of ambient ionization produced by the target radiation exceeds the amount produced by atomic collisions.

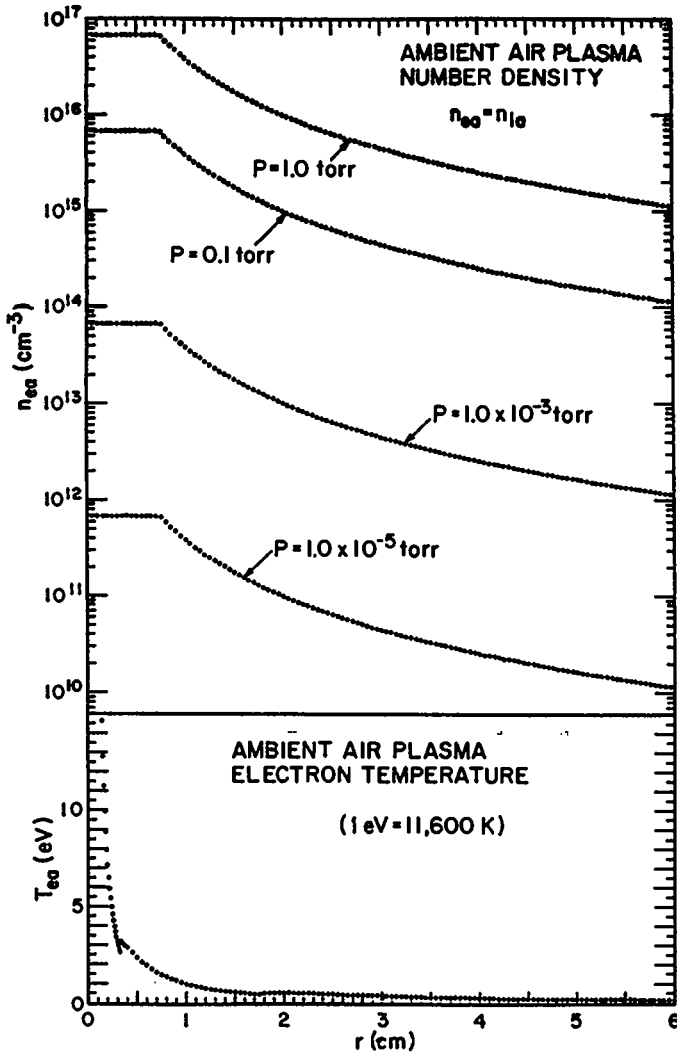


Fig. 14. Peak blackbody photon estimates for the electron number density (top) and electron temperature (bottom) as functions of the radius attributed to ionization by the 150 J of 100-eV target radiation passing through air.

Fig. 15. The air ionization at three instances of time produced because of atomic collisions when 300 J of Maxwellian gold ions ( $T_i = 1.29 \times 10^7$  eV) are released at time  $t = 0$  from the target pellet into 0.1 torr of air. This is compared with the flash ionization produced by 150 J of 100-eV blackbody radiation (as in Fig. 14).

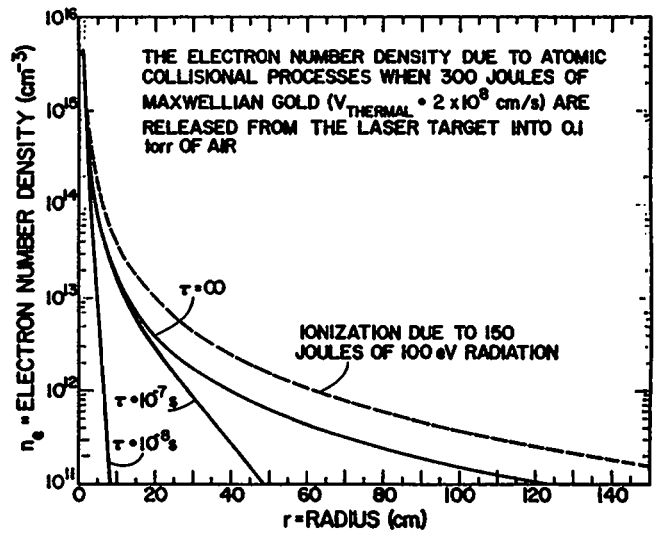


TABLE I

AN ANALYSIS OF 21 FRAMES OF (PLUS-X PAN) STILL CAMERA DATA<sup>a</sup>

Shot Number	Ambient Gas Species	Chamber Pressure (torr)	Macbeth Density	Film Exposure (ergs/cm <sup>2</sup> )	Source Energy (J)	Energy Fraction Observed
1902	Air	4x10 <sup>-3</sup>	1.57	0.501	6.6x10 <sup>-2</sup>	1.4x10 <sup>-5</sup>
1903	Air	4.2x10 <sup>-3</sup>	1.55	0.447	5.9x10 <sup>-2</sup>	1.2x10 <sup>-5</sup>
1904	Air	0.2	0.53	0.776	1.0x10 <sup>-1</sup>	2.2x10 <sup>-5</sup>
2002	Air	0.2	0.50	0.708	9.4x10 <sup>-2</sup>	2.3x10 <sup>-5</sup>
2003	Air	0.2	0.51	0.724	9.6x10 <sup>-2</sup>	2.1x10 <sup>-5</sup>
2004	Air	0.5	0.60	1.047	1.4x10 <sup>-1</sup>	3.0x10 <sup>-5</sup>
2005	Air	0.5	0.73	1.738	2.3x10 <sup>-1</sup>	4.7x10 <sup>-5</sup>
2006	Air	1.0	0.62	1.122	1.5x10 <sup>-1</sup>	3.1x10 <sup>-5</sup>
2007	Air	1.0	0.49	0.676	9.0x10 <sup>-2</sup>	1.8x10 <sup>-5</sup>
2008	Air	1.0	0.63	1.202	1.6x10 <sup>-1</sup>	3.3x10 <sup>-5</sup>
2009	Air	5.0	0.70	1.549	2.1x10 <sup>-1</sup>	4.0x10 <sup>-5</sup>
2012	Argon	1x10 <sup>-3</sup>	0.75	0.186	2.5x10 <sup>-2</sup>	4.6x10 <sup>-6</sup>
2013	Argon	0.1	1.27	1.349	1.8x10 <sup>-1</sup>	4.0x10 <sup>-5</sup>
2105	Argon	0.5	0.84	2.69	3.6x10 <sup>-1</sup>	7.3x10 <sup>-5</sup>
2106	Argon	1.0	1.73	10.47	1.4	2.7x10 <sup>-4</sup>
2107	Argon	3.0	1.93	25.12	3.3	6.9x10 <sup>-4</sup>
2108	Argon	1.0	0.82	0.251	3.3x10 <sup>-2</sup>	7.6x10 <sup>-6</sup>
						(No Target)
2109	Argon	1.0	1.40	2.188	2.9x10 <sup>-1</sup>	7.8x10 <sup>-5</sup>
2110	Argon	1.0	1.77	12.51	1.7	3.7x10 <sup>-4</sup>
2111	Argon	4x10 <sup>-6</sup>	0.34	0.003	4.0x10 <sup>-4</sup>	1.1x10 <sup>-6</sup>
2112	Argon	3x10 <sup>-6</sup>	0.68	0.014	1.9x10 <sup>-3</sup>	2.9x10 <sup>-6</sup>

<sup>a</sup>Assuming isotropic emission, the source energy within the observation cone was calculated from the film exposure using the camera equation. Because the calibration film and the shot film were not processed simultaneously, factor of two uncertainties can be assumed.

### B. Debris Ions

This section describes the modeling of energetic debris ions used to estimate their velocity distribution and to obtain their average charge state.

At any point in time and space outside of the target, time-of-flight velocity selection insures that the expanding collisionless debris ions will be very cold. This is demonstrated as follows. If the debris ions are produced in the vicinity of the target ( $r < r_0$ ) over a finite period from time  $t = 0$  to time  $t = \Delta t$ , then the maximum velocity that a debris ion can have at a point in space and time is given by the maximum distance between the point and any point within the target divided by the minimum time the debris ion could have existed



$$Z_{\text{eff}}^2 = \frac{\left(\frac{dE}{dx}\right)_{\text{ion}}}{\left(\frac{dE}{dx}\right)_{\text{proton}}}$$

As shown in Appendix D, for gold with a velocity of  $2 \times 10^8$  cm/s passing through nitrogen gas (any pressure), the root-mean-squared level of ionization is

$$Z_{\text{eff}} = 5.03$$

In this average state the gold debris ions are five-times ionized. Similar considerations for  $2 \times 10^8$  cm/s aluminum passing through air yield an effective ionization level of

$$Z_{\text{eff}} = 3.48$$

### C. Collisional Effects on the Expansion

To distinguish between collisional and collisionless coupling, it is imperative that the collisional effects be estimated. Using the above models for the background plasma and the debris ions, the collisionality of the expansion of the debris ions through the background air plasma is investigated.

Three processes may lead to the slowing down of a particle passing through an ionized medium: (1) atomic and nuclear collisions, (2) Coulomb collisions, and (3) the Cerenkov emission of plasma waves. The slowing down of a particle in the first process arises from ionizing collisions with orbital electrons (atomic) and inelastic collisions with nuclei (nuclear); the slowing down attributed to Coulomb collisions arises from the sum of many small-angle scatterings from collisions with the free electrons and ions within a Debye sphere of the particle; and the slowing down attributed to Cerenkov emission arises from collective interactions between the imperfectly shielded particle and the surrounding plasma. These three processes are analyzed in Appendix C.

All three processes are comparable for gold traveling at  $2 \times 10^8$  cm/s through air, the Coulomb scattering having the largest effect (Fig. 16). The ranges of  $2 \times 10^8$  cm/s gold traveling in 0.1 torr of air (fully ionized with  $T_e = 1$  eV and  $T_i = 0.2$  eV) because of three processes are (from Appendix D)

R = 1520 cm     atomic and nuclear collisions

R = 516 cm     multiple Coulomb scattering

R = 1570 cm     Cerenkov plasma wave emission

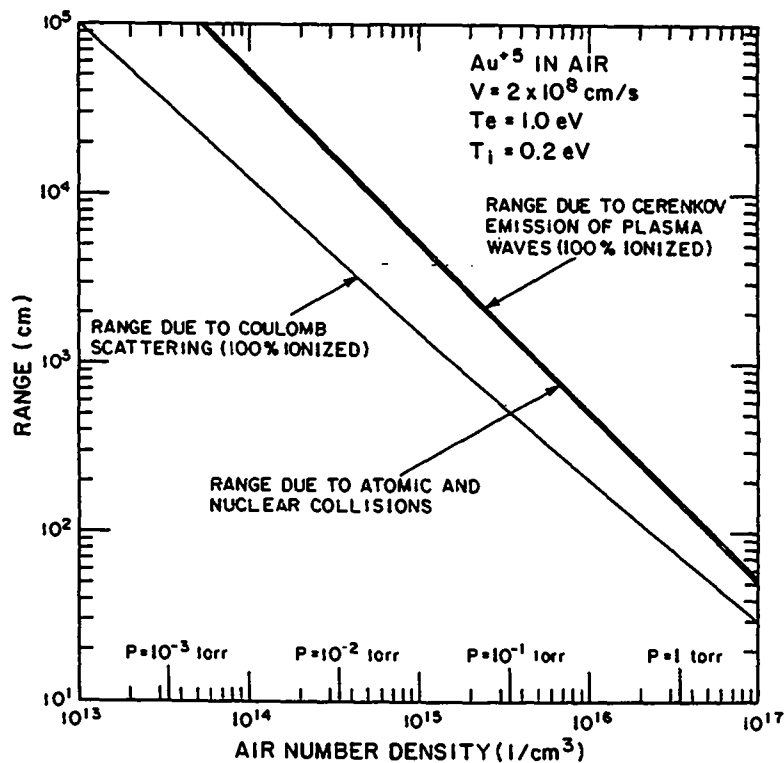


Fig. 16. The ranges attributed to Coulomb scattering, Cerenkov emission, and atomic and nuclear scattering for fifth-ionized gold traveling at  $2 \times 10^8$  cm/s through various pressures of air. The air is assumed to be 100% ionized for the Coulomb and Cerenkov ranges.

With 300 J of debris kinetic energy the equal-mass radius of the experiment is 0.60 cm, hence the shortest range (because of multiple Coulomb scattering) is equal to 860 equal-mass radii. Thus the debris expansion into the 0.1-torr air plasma is collisionless. The time-of-flight ion detectors 175 cm from the target find the shape of the debris-ion velocity distribution function to be invariant as the background air pressure changes, corroborating the fact that the ion expansion is collisionless.

Using an aluminum-coated rather than a gold-coated target, the Helios experiment would be collisionless to the same degree as are the high-altitude bursts lying along the 300-J curve of Fig. 1, the range of a particle divided by the equal-mass radius being the same in the laboratory as in the high-altitude burst. Because the above-mentioned slowing-down processes are so sensitive to the debris velocity, and because these processes scale correctly provided velocities are preserved (see Appendixes A and D), it is very important for a laboratory simulation to obtain the same debris velocities as those occurring in the high-altitude burst. For debris velocities in the vicinity of  $2 \times 10^8$  cm/s, the ranges of these three processes have the following velocity sensitivities:

$$R \propto v^{1.038} \quad \text{atomic and nuclear collisions}$$

$$R \propto v^4 \quad \text{Coulomb collisions}$$

$$R \propto v^4 \quad \text{Cerenkov emission}$$

Thus, to maintain a collisionless experiment, it is very important to maintain high debris velocities.

#### D. Collisional Effects on Air Plasma

Another effect of Coulomb scattering is the thermalization of plasma particles leading to effective collision frequencies. The thermal-relaxation time  $\tau_s$  because of multiple Coulomb scattering may be obtained from a Fokker-Planck test-particle calculation [Equations (D-2) - (D-4)] to yield an effective collision frequency for the plasma particles,  $f_{\text{coll}} = 1/\tau_s$ . As relevant examples, the ion-ion, electron-electron, and ion-electron collision frequencies for 0.1 torr of 100% ionized air plasma with  $T_e = 1$  eV and  $T_i = 0.2$  eV are, respectively,

$$f_{i-i} = 3.1 \times 10^9 \text{ s}^{-1}$$

$$f_{e-e} = 6.3 \times 10^{10} \text{ s}^{-1}$$

$$f_{i-e} = 1.0 \times 10^6 \text{ s}^{-1} \quad .$$

Note that the ion-ion collision frequency for the air is higher than the ion-plasma frequency  $f_{pi} = (n_i e^2 / \pi m_i)^{1/2}$  of air,

$$f_{i-i} = 1.4 f_{pi} \quad .$$

This indicates that magnetized and unmagnetized ion-ion streaming instabilities, which have growth rates comparable to ion-plasma frequencies, may be heavily damped by collisions. Wave theories neglecting these collisional effects may be invalid because collisions cause the particle distribution functions to change rapidly compared with the plasma phenomena of interest. Varying the density of the air does not easily remedy this situation because

$$\frac{f_{i-i}}{f_{pi}} \propto n_e^{1/2} \quad .$$

Decreasing the density by a factor of 100 still leaves  $f_{i-i} = 0.14 f_{pi}$ . The ratio of the ion-ion collision frequency to the ion-plasma frequency may be lowered by a heating of the air ions, as depicted in Fig. 17, but this is not likely. The air ions produced by radiation deposition are probably very cold and they do not have time to be heated by the warmer air electrons before the debris arrives. They may, however, be collisionally heated by nuclear elastic scattering with the high-energy debris ions, but this process may also invalidate collisionless coupling theories because the heating may alter distribution functions on time scales faster than ion-plasma periods.

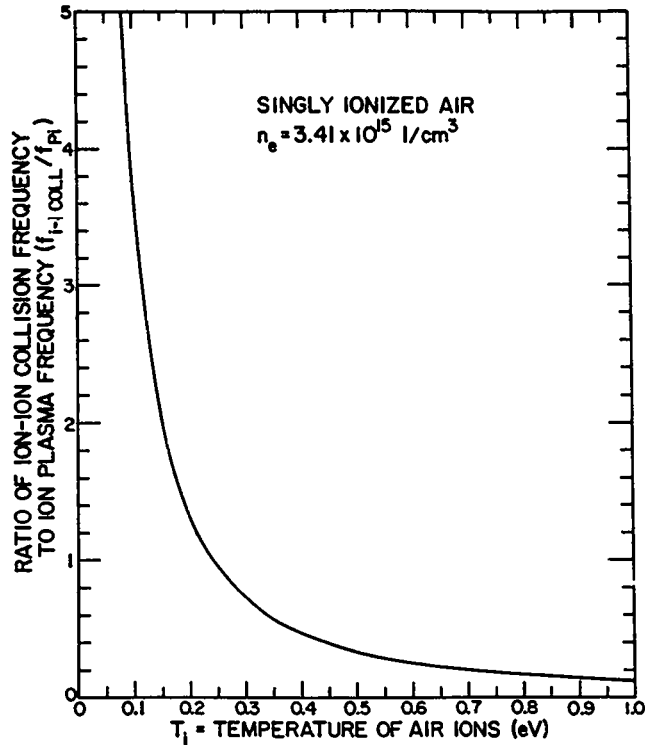


Fig. 17. The ratio of the effective ion-ion collision frequency for air to the ion-plasma frequency for air as a function of the temperature of air ions. The ion-ion collision frequency is obtained from  $f_{coll} = 1/\tau_s$ , the slowing-down time  $\tau_s$  obtained from a Fokker-Planck thermal test-particle calculation (see Appendix D), and the ion-plasma frequency is given by  $f_{ip} = (n_i e^2 / \pi m_i)^{1/2}$ . The density is taken to be  $3.41 \times 10^{15} \text{ cm}^{-3}$  and 100% singly ionized air is assumed.

The importance of these collision frequencies is related to the plasma parameter  $g$ , which is defined as

$$g = \frac{1}{n_e \lambda_{De}},$$

$\lambda_{De}$  being the electron Debye length. Taking the appropriate limit of Eq. (D-3) for the ion Coulomb scattering of a test air ion traveling with one thermal velocity through singly ionized air ions yields the estimate

$$\frac{f_{i-i \text{ coll}}}{f_{pi}} = \left( \frac{T_e}{T_i} \right)^{3/2} g \log\left( \frac{12}{g} \right) ,$$

where  $f_{i-i \text{ coll}} = 1/t_g$  is used. For 0.1 torr of fully ionized air with  $T_e = 1$  eV, there is only an average of 29.4 particles per Debye sphere and the plasma parameter is

$$g \approx \frac{1}{7} .$$

Modeling of the air plasma and of the outwardly expanding debris ions has provided a basis for collisional calculations within the Helios chamber. As is true for the HANE, the expansion of the high-velocity debris through ionized air was found not to be dominated by collisions. However, collisions may have a strong influence on ion-plasma modes, the time scale for thermal relaxation of the air ions being shorter than the air-ion-plasma frequency; this is not true for the high-altitude bursts. At an altitude of 240 km, the number densities are about  $2 \times 10^9 \text{ cm}^{-3}$  and ion-ion collision frequency  $f_{i-i}$  is much lower than the ion-plasma frequency  $f_{pi}$ .

## V. COMPARISON WITH OTHER LASER EXPERIMENTS

The possibility of using laser-exploded plasmas to simulate bomb debris has been realized for some time. Earlier experiments were not spherically symmetric and were collision dominated. But with the development of high-energy lasers, better simulations have become feasible. The Helios  $\text{CO}_2$  laser, with sufficient debris kinetic energy and debris-ion velocities approximating those of a weapon ( $\sim 2 \times 10^8 \text{ cm/s}$ ), presents for the first time the possibility of simulating the Fish Bowl events in the collisionless regime.

The production of debris ions using a high-energy shorter wavelength (1.06- $\mu\text{m}$ ) Nd-glass laser is much less efficient than using a  $\text{CO}_2$  laser; i.e., fewer ions and lower ion velocities result. The relationship between maximum ion velocity  $v_i$ , laser wavelength  $\lambda$ , and effective irradiance  $\Phi_L$  has been established experimentally<sup>7</sup> to be

$$v_i \propto (\lambda^2 \Phi_L)^{1/6} .$$

In an isothermal expansion model the ion sound speed  $c_s$ , representing the bulk ion motion, can also be approximated as

$$c_s \propto v_i \propto (\lambda^2 \Phi_L)^{1/6} .$$

With the same laser irradiance on target, the velocities of the fast ions emitted from a sub-100 ps, 1.06- $\mu\text{m}$  Nd-glass laser pulse are about 2.15 times lower than the fast-ion velocities obtained from a  $\text{CO}_2$  laser pulse. Further, for a sub-100 ps, glass laser pulse the available laser energy is limited to less than 100 J per beam. To operate at higher energies, the glass laser temporal pulses have to be lengthened; a 500-J beam typically requires a pulse length of  $\sim 1$  ns. However, at high irradiance ( $>10^{15}$  W/cm<sup>2</sup>), it is found that the 1.06- $\mu\text{m}$  laser energy can not be effectively coupled to a target during a 1-ns pulse duration because of Brillouin scattering. Hence, in a high-energy Nd-glass laser facility, the production of ions in the velocity range near  $1 \times 10^8$  cm/s and above is suppressed. The bulk of the ion energy conversion from the laser must therefore occur at lower laser irradiances, which results in lower ion velocities ( $\sim 10^7$  cm/s). The simulation of collisionless Fish Bowl events is therefore much less straightforward, if not impossible. The reducing effects on the ion acceleration owing to the presence of background gas is equally applicable to the 1.06- $\mu\text{m}$  Nd-glass laser-target interaction and the total ion kinetic energy available for simulations is further reduced.

## VI. CONCLUSIONS AND RECOMMENDATIONS

### A. Conclusions

The Helios laser experiment has demonstrated that high-power  $\text{CO}_2$  lasers can produce enough debris ions with the proper velocities in the presence of air to simulate the early time effects of HANE. A comparison of the experimental results with the simulation criteria of Sec. I demonstrates the success of the experiment:

- (1) Ion velocity-distribution functions obtained in the experiment have the important  $2 \times 10^8$  cm/s expansion velocities that match the expansion velocities of weapons. Further, the velocity-

distribution functions may be adjusted by varying the target properties.

- (2) Pre-ionization of ambient chamber air is achieved, as evidenced by fiber-optic data and modeling of ionization arising from the target radiation and collisions with the expanding debris ions. The ionization from collisional processes will scale properly, the ionization from target radiation probably does not.
- (3) Spherical symmetry of the explosion is confirmed by multiple calorimeters.
- (4) Sufficient debris-ion energy for scaling the experiment to the HANE of interest is obtained. At 0.1 torr of background air pressure, the experiment follows the 300-J curve of Fig. 1.

Thus the Helios experiment meets all the criteria for a HANE simulation.

An important advantage to preserving the velocities is the fact that the fractional ionization of the air, arising from collisional processes with the debris, is conserved in scaling the experiment up to the high-altitude burst. Equally important, preserving the velocities results in a preservation of the kinematics of collisions so that the velocities of the collision products are preserved, resulting in the same temperatures for collisionally produced plasmas in the laboratory and in the high-altitude burst.

In the Helios experiment, however, the target radiation poorly simulates the radiation produced by a weapon. Whereas the radiant energy of a 1-Mt weapon exceeds the debris kinetic energy, with 0.1 torr of air in the chamber the radiant energy of the Helios laser target (150 J) is less than the kinetic energy of the debris ions (300 J). Because the scaling of the laser experiment to the high-altitude bursts is governed by the ratio of the debris kinetic energy of the experiment to the debris kinetic energy of the weapon, the radiation yields do not scale unless the ratio of the debris kinetic energy to the radiant energy is the same for the laser experiment as it is for the weapon. This ratio, in fact, worsens as the air pressure in the laser chamber decreases. A less serious error in simulating the weapon radiation with the laser-target radiation lies in the difference in blackbody temperatures. Consider a 1-Mt weapon having a hypothetical radiation temperature on the order of 1 keV, whereas the Helios target has a radiation temperature on the order of 100 eV. Although the laser target produces photons that are a factor of 10 less energetic than those produced by the weapon, this error is tempered by the

fact that the opacity to the lower energy photons is a factor of 10 or more higher than the opacities for the weapon photons.

Under the conditions of the experiment (collisionless, spherical expansion, zero magnetic field), the debris ions were not significantly coupled to the ambient air plasma. This result agrees with the results of earlier laser-plasma experiments,<sup>10</sup> none of which, however, were spherically symmetric. Collisionless coupling mediated by unmagnetized ion-ion streaming instabilities is not expected to occur in the experiment because (1) the electron temperatures of the air plasmas are cool allowing the electrons to effectively shield any space charge resulting from ion clumping, and (2) the collision frequencies for air ions are higher than the ion-plasma frequencies of the air.

### B. Recommendations

Preservation of the debris velocity in a simulation ensures that the degree of collisionality is preserved when the experiment is scaled to a HANE (see Appendix A). Because collisional processes such as multiple Coulomb scattering are very sensitive to the debris velocity, it is important to match the experimental velocities to weapon velocities.

The importance of preserving the debris velocity is stressed by an examination of aluminum ions passing through air. The ranges of aluminum ions limited by multiple Coulomb scattering and limited by atomic and nuclear collisions in 0.1 torr of air all decrease by over an order of magnitude as the velocity is reduced from  $2 \times 10^8$  cm/s to  $4 \times 10^7$  cm/s (see Fig. 18). The magnitude of decrease in the Coulomb scattering range is very sensitive to the electron temperature of the air plasma; as Fig. 19 shows, fourth-ionized aluminum debris ions with velocities of  $2 \times 10^8$  cm/s have ranges greater than 100 cm for 0.1 torr of fully ionized air with realistic electron temperatures, but fourth-ionized aluminum debris ions with velocities of  $4 \times 10^7$  cm/s have ranges that decrease to less than 1 cm as the electron temperature decreases much below 1 eV. In this example, Coulomb scattering may dominate the early time dynamics of a laser experiment (whereas it does not in a HANE) if the debris velocities are not preserved.

The Helios laser experiment is capable of simulating 1-Mt bursts at altitudes of 240 km or higher, the lower altitude limit corresponding to 0.1 torr of air in the laser chamber. At pressures near 0.1 torr, a fully ionized air plasma with ion temperatures of 0.2 eV suffers from the drawback that the thermal-relaxation time for the air ions is shorter than the air ion-plasma

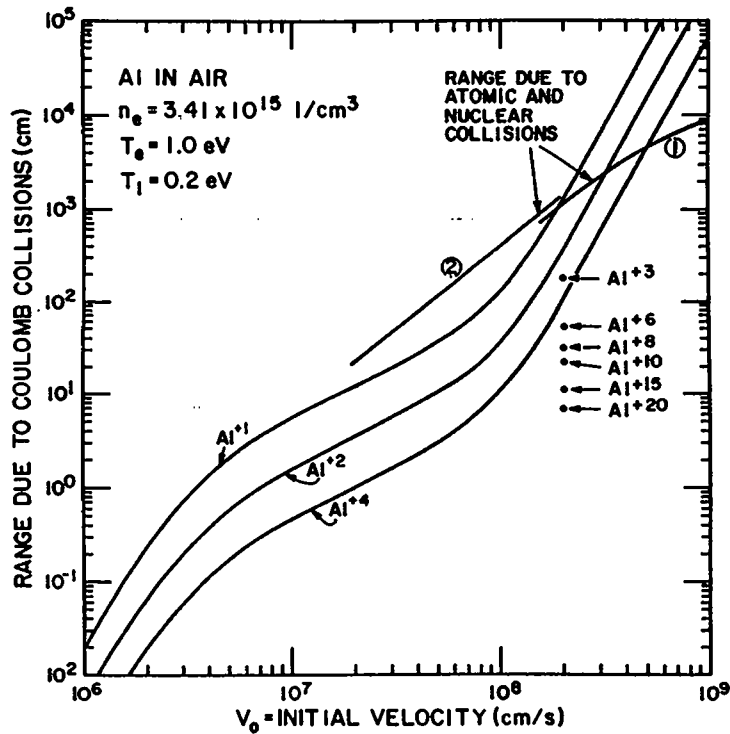


Fig. 18. The ranges of variously ionized aluminum ions arising from multiple Coulomb scattering as they pass through an air plasma with an electron number density  $n_e = 3.41 \times 10^{15} \text{ cm}^{-3}$ , an electron temperature  $T_e = 1.0 \text{ eV}$ , and an ion temperature  $T_i = 0.2 \text{ eV}$  as functions of their velocity. These ranges are compared with the ranges attributed to atomic and nuclear collisions with the air; curve (1) is obtained from Fig. 4.14 of Ref. 12 and curve (2) is obtained from Ref. 14.

period and the simulation of collisionless coupling by ion-ion streaming instabilities is dubious. Therefore, simulations of bursts at the lowest allowable altitudes should be avoided.

Having spherically symmetric bursts of debris ions in the laser experiment is very advantageous if the structure generated by early time coupling is to be studied, these structures seeding late time structures. The origin of structure obtained from nonsymmetric bursts will be ambiguous. The capability to produce spherically symmetric debris bursts is of particular importance when an external magnetic field is added to the experiment, electrical current systems that are due to spherical expansions dominating the dynamics of a HANE. If the spherical symmetry is forsaken in an experiment, large-scale polarization charging may dominate the dynamics of the debris expansion.

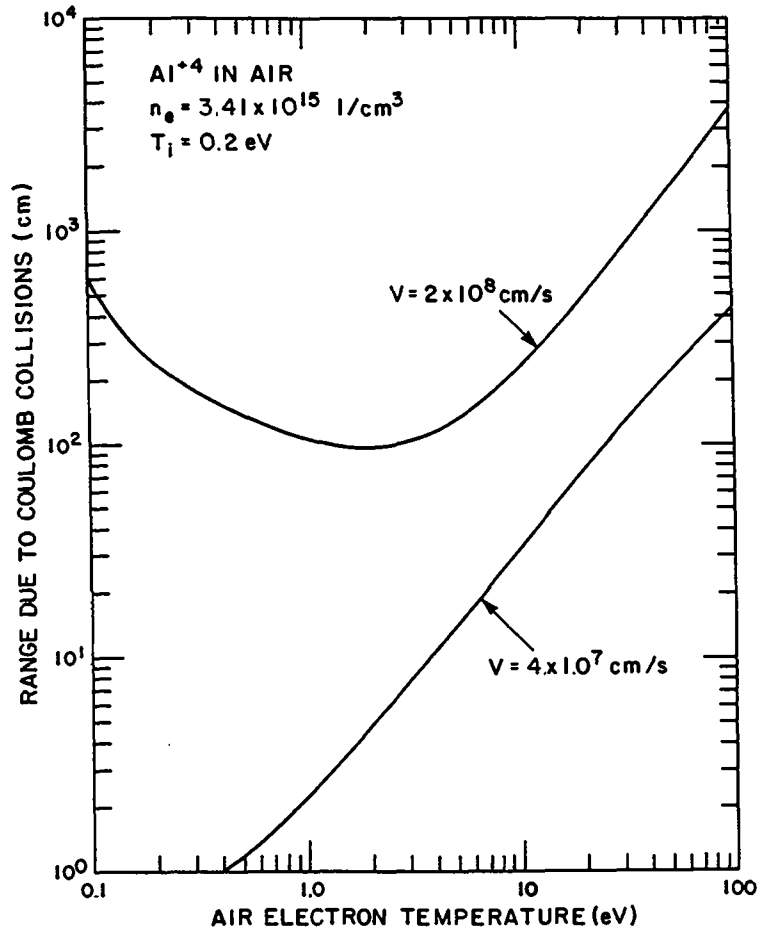


Fig. 19. A comparison of the ranges arising from multiple Coulomb scattering of fourth-ionized aluminum ions streaming with velocities of  $2 \times 10^8 \text{ cm/s}$  and of  $4 \times 10^7 \text{ cm/s}$  through an air plasma with electron number density  $n_e = 3.41 \times 10^{15} \text{ cm}^{-3}$  and ion temperature  $T_i = 0.2 \text{ eV}$  as functions of the electron temperature.

#### ACKNOWLEDGMENTS

The authors wish to acknowledge John Kephart, Erick Lindman, Henn Oonna, Sidney Stone, Kenneth Winn, the Helios laser operation crew, and the target fabrication personnel for their aid in the experiment; Richard C. Anderson, Steven G. Blair, S. Peter Gary, and Robert A. Roussel-Dupre for their aid in the analysis; and R. Stellingwerf for his simulation of ion emission from CO<sub>2</sub> laser interactions.

Conversations with Arthur W. Ehler, Philip Goldstone, Dale S. Sappenfield, David J. Simons, Michelle F. Thomsen, and David T. Young (of Los Alamos) and M.

Alme and Conrad Longmire (of Mission Research Corporation) are gratefully acknowledged.

. .  
. .

.  
.

APPENDIX A  
SCALING RELATIONS

This appendix summarizes the scaling relations appropriate for the Helios simulation experiment.

Cases where strong coupling is expected between the expanding debris and the ambient air should scale according to inertial (hydrodynamic) scaling. Because the velocities of the debris and ambient air plasma are preserved in the Los Alamos experiment, and because debris of the same composition as that of a weapon may be used, the appropriate scaling is the inertial scaling appearing in the Longmire et al. report.<sup>2</sup> One great advantage of the preservation of the velocities is that the degree of collisionality is preserved along with such important quantities as the fractional collisional ionization of the air and the charge level of the debris.

INERTIAL SCALING

Defining Y to be the scale factor for the kinetic energy yield

$$Y = \frac{\text{kinetic energy of experimental debris}}{\text{kinetic energy of bomb debris}},$$

preserving the scaling of the equal-mass radii (radii where the debris have swept through their mass in ambient media) results in scale factors for the mass  $M'$ , radius  $r'$ , mass density  $\rho'$ , number density  $n'$ , and time  $t'$  given by<sup>2</sup>

$$M' = Y = \frac{\text{mass in experiment}}{\text{mass in high-altitude event}}$$

$$r' = Y^{1/2} = \frac{\text{radius in experiment}}{\text{radius in high-altitude event}}$$

$$\rho' = Y^{-1/2} = \frac{\text{mass density in experiment}}{\text{mass density in high-altitude event}}$$

$$n' = Y^{-1/2} = \frac{\text{number density in experiment}}{\text{number density in high-altitude event}}$$

## THE SCALING OF COLLISIONAL PROCESSES

We define the collisionality of a species of particles to be the ratio of the particle range  $R$  to the equal-mass radius (inertial radius)  $r_{\text{eq mass}}$ ,

$$C = \frac{R}{r_{\text{eq mass}}},$$

the equal-mass radius being the radius of a sphere that contains a mass of air equal to the total mass of the outflowing debris. If the velocities are preserved in the simulation then, for nuclear collisions, for atomic collisions, for multiple Coulomb collisions, and for Cerenkov plasma processes, the range  $R$  of a particle traveling through a medium with number density  $n$  is of the form

$$R = \frac{\text{constant}}{n}.$$

Hence the collisionality  $C$  of that species of particles is of the form

$$C = \frac{\text{constant}}{n r_{\text{eq mass}}}.$$

Using the scaling factors  $n'$  and  $r'$  for the number density and radius,

$$n' = \gamma^{-1/2}$$

$$r' = \gamma^{1/2},$$

leads to the collisionality scaling factor

$$C' = 1.$$

(A-1)

Thus, the degree of collisionality of the simulation is the same as the degree of collisionality of the high-altitude explosion, provided the velocities are preserved in the simulation.

Likewise the degrees of collisional ionization of the debris and the air plasma are also preserved if the velocity of the debris is preserved. The degree of ionization of the air plasma is calculated as follows. The number of ionizations produced by one debris ion traveling a distance  $r$  from the target is given by

$$N_{\text{one debris ion}} = n_{\text{air}} \sigma_{\text{ionz}} r ,$$

where  $n_{\text{air}}$  is the number density of air in the chamber and where  $\sigma_{\text{ionz}}$  is the total ionization cross section (which is preserved by preserving the debris velocity). The total number of ionizations that are due to all of the debris ions traveling a distance  $r$  from the target is given by

$$N_{\text{all debris ions}} = \frac{M_{\text{debris}}}{m} n_{\text{air}} \sigma_{\text{ionz}} r ,$$

where  $M_{\text{debris}}$  is the total debris mass and where  $m$  is the mass of one debris ion (preserved). The number density of collisionally created ionizations is obtained by dividing the total number of ionizations by the volume,

$$n_{\text{ionz}} = \frac{\frac{M_{\text{debris}}}{m} n_{\text{air}} \sigma_{\text{ionz}} r}{\frac{4}{3} \pi r^3} .$$

The fraction of ionization  $F_{\text{ionz}}$  of the air is obtained by dividing the number density of ionizations  $n_{\text{ionz}}$  by the number density of air  $n_{\text{air}}$ ,

$$F_{\text{ionz}} = \frac{\sigma_{\text{ionz}} M_{\text{debris}}}{\frac{4}{3} \pi r^2 m} .$$

We define a scale factor  $F'_{\text{ionz}}$  for the fraction of ionization as

$$F'_{\text{ionz}} = \frac{\text{fractional ionization of air in experiment}}{\text{fractional ionization of air in high-altitude event}}$$

Because  $M_{\text{debris}}$  scales as  $Y$  and  $r$  scales as  $Y^{1/2}$ , and since  $\sigma_{\text{ionz}}$  and  $m$  are preserved, the degree of ionization of the air scales as

$$F'_{\text{ionz}} = 1 \quad , \quad (\text{A-2})$$

hence, the degree of air ionization is preserved because the debris velocity is preserved.

Preserving the debris velocity (and type of debris) preserves the charge state of the debris ions as they stream through air. As explained in Appendix D, this is because the level of ionization of a given particle streaming through a given medium is a function only of its velocity, not of the number density of the medium.

Preserving the debris velocities also ensures that the kinematics of two-body atomic collisions are preserved, yielding the same velocity products, ensuring that such quantities as the electron temperatures of collisionally created air plasmas are preserved.

## APPENDIX B DETECTORS

This appendix contains a brief description of the major detectors used in the Helios experiment at Los Alamos National Laboratory.

**CALORIMETERS**-- Over 20 calorimeters are employed at various spatial locations in the Helios experiment. Each calorimeter, a 10-cm<sup>2</sup> area of chromel-constantan thermocoupling material several mils in thickness, measures the total kinetic energy of all particles and photons that it absorbs. Essentially all of the incident particles are absorbed, but hard x rays pass through these detectors and do not register. The temperature of the thermocouple correlates with an electrical potential between two different alloys, the temperature-voltage response having been experimentally calibrated. This response has no time resolution and is a measure of the total energy that the pellet receives from the laser.

**THRESHOLD CALORIMETERS**-- Some of the calorimeters used in the Helios experiment are threshold calorimeters, identical to those described above but shielded by a 0.5- $\mu$ m nickel foil that prevents hydrogen ions with velocities less than 2 to  $5 \times 10^8$  cm/s and gold ions with velocities less than 1.5 to  $2.5 \times 10^8$  cm/s from registering on the calorimeter and that also screens out ultraviolet radiation. By comparing the responses of these shielded calorimeters with those of unshielded calorimeters, a measurement of the total kinetic energy of the fast target ions is obtained.

**CHARGE CUPS**-- The charge cup employed in the Helios experiment measures the flux of energetic ions reaching the chamber wall. The 0.8-cm<sup>2</sup> face of the cup is covered by a 0.5- $\mu$ m nickel foil that prevents plasma from entering the cup. This foil transmits hydrogen ions and neutrals with velocities approximately greater than 2 to  $5 \times 10^8$  cm/s and transmits gold ions and neutrals with velocities approximately greater than 1.5 to  $2.5 \times 10^8$  cm/s, stripping them of an unknown number of electrons as they pass. Upon striking a negatively biased metal collecting plate at the back of the cup, a transmitted particle is neutralized and a current is registered as a voltage drop across a 50- $\Omega$  resistor. This voltage is sent to an oscilloscope where time-resolved particle fluxes may be inferred. Inaccuracies in the measurement are due primarily to

the unknown ionization level of the transmitted particles and due to the escape of secondary electrons that are produced by ion impact on the metal collector, an escaping electron being misinterpreted as an incoming ion. The charge cup is also sensitive to photons of high enough energy to pass through the nickel foil and produce photoelectric electrons from the collector, a burst of electromagnetic radiation appearing as a burst of incident ions.

FIBER OPTICS-- Two fiber-optic devices are used in the Helios experiment. These consist of quartz fibers that conduct infrared, viable, and ultraviolet radiation from the inside wall of the target chamber to photomultipliers outside. The (uncalibrated) photomultipliers respond to viable wavelengths, peaking in sensitivity at 3900-4000Å. The half-angle view of each fiber is  $11.5^\circ$ . One fiber views the target, the other is directed  $35^\circ$  away so that its center of view has an impact parameter of about 1.1 m with the pellet (see Fig. 9). The voltage output of the photomultipliers is related to the flux into the fibers, these voltages sent to oscilloscopes for a time resolution of approximately  $10^{-8}$  s. Deconvolving the fields of view yields time-of-flight information about sources of visible radiation.

CRAB EYE-- The crab-eye detector employed in the Helios experiment is a scintillator-photomultiplier used to measure the velocity of the fastest ions present. The scintillation material is a thin slab of low-Z polyvinyl toluene (N.E.102) with a poor efficiency for photon detection, although low-energy x rays will register. The detector is located a distance of 3 m from the target pellet in an extension to the chamber. The time resolution of this detector is  $1.5$  to  $2.0 \times 10^{-9}$  s. Because of the very high time resolution, the crab-eye detector is only in operation for a short time interval during an experiment, an interval too brief for particles with velocities of  $10^8$  cm/s or less to reach the detector and be measured.

STILL CAMERAS-- Two time-integrated film cameras are employed to photograph the near field (1-cm-diam at the target) and the far field ( $\sim 2$ -m-diam at the target) phenomena. One camera is a Hasselblad Model 500 EL (located at  $r = 220$  cm, viewing the entire chamber) with a 50-mm focal length objective operated with an f/22 aperture setting. Plus-X Professional Pan (ASA 125) (2-1/4" x 2-1/4") film is used and the film was hand processed in D-76 developer for 5 min at  $70^\circ\text{f}$ , a radiometric stepwedge also produced and

processed similarly. The film density is measured with a Macbeth densitometer with a spot size corresponded to a diameter of 13 cm at the target, the film densities converted to film exposure using the stepwedge calibration.

HIGH-VOLTAGE PROBE-- This probe is a low-capacitance and low-inductance voltage-divider circuit with a resistance of 50  $\Omega$ . The laser target return current from ground is sampled in a 0.005- $\Omega$  section of the circuit that is connected to a low-loss and low-dispersion foam-flex coaxial cable and the signal is recorded on a fast 3-GHz oscilloscope.

NEUTRON DETECTORS-- These are neutron-sensitive scintillator-photomultiplier detectors with time resolutions of a few nanoseconds. The scintillation material is a cylinder of N.E.111 plastic 2 in. in diameter and 2 in. in length and the photomultiplier is a low-noise ultrafast XP2020 10-stage tube.

APPENDIX C  
ESTIMATES OF AIR PLASMA PARAMETERS

This appendix describes models for estimating the density and electron temperature of a plasma created by the electromagnetic radiation from the hot target interacting with the ambient air and by collisional processes during an outflow of target debris.

FROM FLASH IONIZATION

We first consider the simplest model: that a sphere of uniform ionization is produced by the radiation. This will provide an estimate of the maximum amount of ionization. An amount of radiated energy  $E$  will produce a number  $N$  of ionizations given by

$$N = \frac{E}{E_{\text{ionz}}},$$

where  $E_{\text{ionz}}$  is the average energy of ionization ( $E_{\text{ionz}} \approx 20$  eV). If a sphere of uniform ionization is produced, then the number density  $n$  of the air plasma is

$$n = \frac{N}{\frac{4}{3} \pi r^3}.$$

If  $F$  is the fraction of ionization  $n/n_{\text{air}}$ , then

$$n = F n_{\text{air}} = F 3.41 \times 10^{16} \text{ cm}^{-3} \frac{P}{1 \text{ torr}},$$

where  $n_{\text{air}}$  is the particle density of the neutral air (80%  $\text{N}_2$  and 20%  $\text{O}_2$ ) before the laser irradiation of the pellet and where  $P$  is the air pressure. Combining these three equations yields the radius of the sphere of fractional ionization produced by an amount of radiated energy  $E$ ,

$$r = 1.22 \text{ cm} \left[ \left( \frac{E}{1 \text{ J}} \right) \frac{1}{F} \left( \frac{1 \text{ torr}}{P} \right) \right]^{1/3} \quad (C-1)$$

A slightly more complicated model yields estimates for the electron temperature and number density of the air plasma as a function of radius. Assuming that a point source emits a pulse of radiation, the radiant energy flux that passes a distance  $r$  from the source is

$$F_R = \frac{E}{4\pi r^2} e^{-\kappa \rho r} \quad (C-2)$$

where  $E$  is the energy of the radiation pulse,  $\kappa$  is the opacity of the gas to the radiation, and  $\rho$  is the mass density of the gas (assumed not to be a function of  $r$ ). The exponential in Eq. (C-2) represents an extinction of the pulse. The radiation energy deposition into the gas as the pulse passes is given by

$$W = F_R \kappa \rho \quad ,$$

or

$$W = \frac{E\kappa\rho}{4\pi r^2} e^{-\kappa \rho r} \quad (C-3)$$

The number density of (single) ionization pairs resulting from the energy deposition into the gas is

$$n_{\text{pair}} = \frac{W}{E_{\text{pair}}} \quad (C-4)$$

where  $E_{\text{pair}}$  is the energy absorbed per ionization pair, which may be approximated by

$$E_{\text{pair}} \approx E_{\text{ionz}} + \frac{3}{2} k_B T_e ,$$

$E_{\text{ionz}}$  being the ionization energy of the gas.

For the Helios experiment we take the radiated energy to be

$$E = 150 \text{ J} .$$

Because the most probable energy of a photon emitted from a blackbody source is given by

$$h\nu = 2.814 k_B T_e ,$$

we use for  $\kappa$  the opacity of 280-eV photons in air,\*

$$\kappa(280 \text{ eV}) = 6.5 \times 10^3 \frac{\text{cm}^2}{\text{g}} ,$$

and the density of air at a pressure  $P$  is given by

$$\rho = 1.6 \times 10^{-6} \frac{P}{1 \text{ torr}} \frac{\text{g}}{\text{cm}^3} .$$

With these values Eq. (C-3) may be integrated out from the laser target to get the energy deposition  $W$  as a function of radius  $r$ . With these results, the

---

\*Information provided by C. D. Sutherland, Los Alamos National Laboratory.

electron thermal energy of the air plasma is obtained by parameterizing the theoretical curves contained in Fig. 2 of Ref. 11 with

$$\begin{aligned}
 T_e &= w' [ 1.1 \times 10^{-10} - 4.3 \times 10^{-12} \log(w') ] \quad \text{for } 1.0 \times 10^{10} < w' < 3.5 \times 10^{10} \\
 T_e &= w' [ 5.2 \times 10^{-11} - 1.9 \times 10^{-12} \log(w') ] \quad \text{for } 3.5 \times 10^{10} < w' < 2.5 \times 10^{11} \\
 T_e &= w' [ 1.1 \times 10^{-11} - 3.7 \times 10^{-13} \log(w') ] \quad \text{for } 2.5 \times 10^{11} < w' < 6.0 \times 10^{12} \\
 T_e &= w' [ 3.7 \times 10^{-13} ] \quad \text{for } 6.0 \times 10^{12} < w' < 2.0 \times 10^{14}
 \end{aligned}
 \tag{C-5}$$

where the dimensionless quantity

$$w' = \frac{W}{\rho} \frac{g}{\text{erg}}
 \tag{C-6}$$

is the number of ergs of energy deposited per gram of air ( $1 \text{ J} = 10^7 \text{ erg}$ ). We estimate the air-ion temperature to be approximately the temperature of the ambient air. Knowing the electron temperature and using  $E_{\text{ionz}} = 20 \text{ eV}$  for the ionization energy for air, Eq. (C-4) yields the number density of electrons and air ions. Example values of the air-plasma number densities and electron temperatures for the 150 J of 100-eV target radiation propagating through the ambient air as functions of the radius are displayed in Fig. 16.

#### FROM ATOMIC COLLISIONS DURING DEBRIS OUTFLOW

The amount of ionization arising from atomic collisional processes when a known distribution of debris ions streams outward through the ambient gas may be obtained with the use of Eq. (C-4),

$$n_{\text{ionz}} = \frac{W}{E_{\text{ionz}}}$$

where  $E_{ionz}$  is the ionization energy of air and where now the time-integrated energy deposition  $W$  as a function of the radius is given by

$$W = \int_0^{\infty} n_{debris} \frac{\partial E}{\partial x} v_{debris} dt \quad ,$$

the debris number density  $n_{debris}$ , the atomic stopping power of a debris ion  $\partial E/\partial x$ , and the velocity of a debris ion  $v_{debris}$  all being functions of both the time and the radius. For a convenient estimate of the atomic stopping power, Eqs. (4-54) and (4-46) of Ref. 12 (see Ref. 13) are used.

APPENDIX D  
COLLISIONAL EFFECTS

In this appendix the ranges and stopping powers for particles passing through ionized media are investigated. For the parameters of the Helios laser experiment it is concluded that both multiple Coulomb scattering and the Cerenkov emission of plasma waves are as important as are atomic and nuclear collisions. Simulations using debris velocities less than  $1 \times 10^8$  cm/s may be collisionally dominated for the background air densities of interest.

ATOMIC AND NUCLEAR COLLISIONS

A high-energy particle passing through neutral matter suffers many inelastic collisions with orbital electrons and many elastic collisions with nuclei, the net result being a loss of kinetic energy from the particle and an ionization and heating of the neutral matter. The range  $R$  of such a particle suffering many collisions with atoms is given by

$$R = \int_E^0 \left( \frac{dE}{dx} \right)^{-1} dx \quad ,$$

$dE/dx$  being the rate of energy loss of the particle denoted the stopping power. Some of the atomic and nuclear ranges (for single particles traveling through un-ionized media) pertaining to the Helios experiment and to the HANE are:

$$\text{Au} \quad v = 2 \times 10^8 \frac{\text{cm}}{\text{s}} \quad (4.1 \text{ MeV}) \quad \text{in } N_2, \quad R \approx 0.20 \text{ cm} \frac{760 \text{ torr}}{P} \quad (\text{Ref. 14})$$

$$\text{W} \quad v = 2 \times 10^8 \frac{\text{cm}}{\text{s}} \quad (3.8 \text{ MeV}) \quad \text{in } N_2, \quad R \approx 0.20 \text{ cm} \frac{760 \text{ torr}}{P} \quad (\text{Ref. 14})$$

$$p^+ \quad v = 2 \times 10^8 \frac{\text{cm}}{\text{s}} \quad (20.9 \text{ keV}) \quad \text{in } N_2, \quad R \approx 0.10 \text{ cm} \frac{760 \text{ torr}}{P} \quad (\text{Ref. 14})$$

$$p^+ \quad v = 1 \times 10^9 \frac{\text{cm}}{\text{s}} \quad (2.1 \text{ MeV}) \quad \text{in } N_2, \quad R \approx 8.0 \text{ cm} \frac{760 \text{ torr}}{P} \quad (\text{Ref. 14})$$

For example, gold ions traveling at  $2 \times 10^8$  cm/s through air at a pressure P of 0.1 torr have an atomic range of 1500 cm.

The energy lost by these high-energy particles shows up primarily as ionization of the ambient air. In traveling the distance to the chamber wall (175 cm), the fraction  $\Gamma$  of the particles kinetic energy going into air ionization is estimated by

$$\Gamma = \frac{1}{E} \frac{dE}{dx} 175 \text{ cm} .$$

With the following values of  $dE/dx$

$$\text{Au } v = 2 \times 10^8 \frac{\text{cm}}{\text{s}} \quad (4.1 \text{ MeV}) \quad \text{in } N_2, \quad \frac{dE}{dx} = 9.02 \frac{\text{MeV}}{\text{cm}} \frac{P}{760 \text{ torr}} \quad (\text{Ref. 14})$$

$$\text{W } v = 2 \times 10^8 \frac{\text{cm}}{\text{s}} \quad (3.8 \text{ MeV}) \quad \text{in } N_2, \quad \frac{dE}{dx} = 8.79 \frac{\text{MeV}}{\text{cm}} \frac{P}{760 \text{ torr}} \quad (\text{Ref. 14})$$

$$p^+ v = 2 \times 10^8 \frac{\text{cm}}{\text{s}} \quad (20.9 \text{ keV}) \quad \text{in } N_2, \quad \frac{dE}{dx} = 0.36 \frac{\text{MeV}}{\text{cm}} \frac{P}{760 \text{ torr}} \quad (\text{Ref. 14})$$

$$p^+ v = 1 \times 10^9 \frac{\text{cm}}{\text{s}} \quad (2.1 \text{ MeV}) \quad \text{in } N_2, \quad \frac{dE}{dx} = 0.134 \frac{\text{MeV}}{\text{cm}} \frac{P}{760 \text{ torr}} \quad (\text{Ref. 14})$$

the following fractions are obtained.

$$\text{Au } v = 2 \times 10^8 \frac{\text{cm}}{\text{s}} \quad (4.1 \text{ MeV}) \quad \text{in } N_2, \quad \Gamma = 365 \frac{P}{760 \text{ torr}} < 1$$

$$\text{W } v = 2 \times 10^8 \frac{\text{cm}}{\text{s}} \quad (3.8 \text{ MeV}) \quad \text{in } N_2, \quad \Gamma = 401 \frac{P}{760 \text{ torr}} < 1$$

$$p^+ v = 2 \times 10^8 \frac{\text{cm}}{\text{s}} \quad (20.9 \text{ keV}) \quad \text{in } N_2, \quad \Gamma = 2980 \frac{P}{760 \text{ torr}} < 1$$

$$p^+ v = 1 \times 10^9 \frac{\text{cm}}{\text{s}} \quad (2.1 \text{ MeV}) \quad \text{in } N_2, \quad \Gamma = 11.1 \frac{P}{760 \text{ torr}} < 1$$

For gold traveling at  $2 \times 10^8$  cm/s through 0.1 torr of air, the fractional energy loss is 4.80%, hence 300 J of  $2 \times 10^8$  cm/s gold debris will deposit about 14.4 J of energy into the 0.1 torr of air in the chamber.

The ionization cross sections for fast electrons are readily available:

$$e^- (100 \text{ eV}) \text{ in } N_2, \quad \sigma_{\text{ionz}} = 2.9 \times 10^{-15} \text{ cm}^2 \quad (\text{Ref. 15})$$

$$e^- (1.1 \text{ keV}) \text{ in } N_2, \quad \sigma_{\text{ionz}} = 7.8 \times 10^{-17} \text{ cm}^2 \quad (\text{Ref. 15})$$

(the second value by extrapolation and the values for  $O_2$  being very close to those for  $N_2$ ). The number of ion pairs created if the electron passes directly from the target to the Helios chamber wall ( $r = 175$  cm) may be estimated through

$$N_{\text{ionz}} = n_{\text{air}} \sigma_{\text{ionz}} 175 \text{ cm} ,$$

yielding

$$(100 \text{ eV}), \quad N_{\text{ionz}} = 1800 \frac{P}{1 \text{ torr}} < 2.8$$

$$(1.1 \text{ keV}), \quad N_{\text{ionz}} = 480 \frac{P}{1 \text{ torr}} < 306 ,$$

where the maximum number of ionization pairs is obtained by allowing 36 eV per ionization (Ref. 16).

As in the case of a HANE, the degree of collisional ionization  $F$  decreases as  $r^{-2}$  because of the  $r^{-2}$  falloff of the flux of debris from a point source. A numerical calculation of the number density of free air electrons produced by atomic collisions as gold debris streams through the ambient air appears in Sec. IV-A.

Another collisional process of interest is charge exchange. While the kinetic energy transfer in charge-exchanging collisions is small, a hindrance of the capability of collective processes to couple plasmas may occur. The

charge-exchange cross sections for hydrogen traveling at  $v = 2 \times 10^8$  cm/s through  $N_2$  gas are

$$H \rightarrow H^+, \quad \sigma_{0 \rightarrow 1} = 2.06 \times 10^{-16} \text{ cm}^2 \quad (\text{Ref. 17})$$

$$H^+ \rightarrow H, \quad \sigma_{1 \rightarrow 0} = 3.86 \times 10^{-16} \text{ cm}^2, \quad (\text{Ref. 17})$$

the cross sections for hydrogen traveling at  $2 \times 10^9$  cm/s being much smaller.<sup>17</sup> The mean free path  $L$  between charge-exchange collisions is given by

$$L = \frac{1}{\sigma n_{\text{air}}},$$

or, assuming the air to be  $N_2$  gas,

$$L = \frac{1}{\sigma 3.41 \times 10^{16}} \frac{1 \text{ torr}}{P},$$

yielding

$$L_{0 \rightarrow 1} = 0.14 \text{ cm} \frac{1 \text{ torr}}{P}$$

$$L_{1 \rightarrow 0} = 0.076 \text{ cm} \frac{1 \text{ torr}}{P}.$$

At a pressure  $P$  of 0.1 torr these mean free paths are  $L_{0 \rightarrow 1} = 1.4$  cm and  $L_{1 \rightarrow 0} = 0.76$  cm, thus the hydrogen particles from the target suffer greatly from charge-exchange collisions and potentially may escape collective coupling during their neutral phase.

Charge-exchanging collisions for gold traveling at  $v = 10^8$  cm/s through air cause the gold ions to fluctuate between highly ionized charge states. An estimate of the average level of ionization  $Z_{\text{eff}}$  of a heavy ion traveling

through a medium is obtained by comparing the stopping power of the heavy ion to the stopping power of protons ( $Z_{\text{eff}} = 1$ ) traveling at the same velocity through the same medium,<sup>9</sup>

$$Z_{\text{eff}}^2 = \frac{\left(\frac{dE}{dx}\right)_{\text{ion}}}{\left(\frac{dE}{dx}\right)_{\text{proton}}} \quad (\text{D-1})$$

For velocities of  $2 \times 10^8$  cm/s, Ref. 14 yields

$$\left(\frac{dE}{dx}\right)_{\text{gold}} = 9.02 \frac{\text{MeV}}{\text{cm}} \frac{P}{760 \text{ torr}}$$

$$\left(\frac{dE}{dx}\right)_{\text{proton}} = 0.36 \frac{\text{MeV}}{\text{cm}} \frac{P}{760 \text{ torr}},$$

and we obtain

$$Z_{\text{eff}} = 5.03$$

as the root-mean-squared ionization level for gold in  $\text{N}_2$  gas, independent of the pressure. Because the charge level of a fast ion depends only on its velocity, all such ionization levels are preserved in velocity-preserving simulations.

#### MULTIPLE COULOMB SCATTERING

Multiple Coulomb collisions of a charged particle streaming through a plasma with the other charged particles within a Debye sphere produce a viscous drag on the streaming particle. The results of a Fokker-Planck calculation<sup>18</sup> for a test particle traveling with velocity  $v_t$  through an ionized medium yield a slowing-down time for the test particle of

$$\tau_s = - \frac{v_t}{\left( \frac{\partial v_t}{\partial t} \right)}, \quad (D-2)$$

where

$$\frac{\partial v_t}{\partial t} = \frac{4\pi n_e e^4 Z_t^2}{m_t^2} \log(\Lambda) \cdot \quad (D-3)$$

$$\cdot \frac{\partial}{\partial v_t} \left\{ \frac{1}{v_t} \left[ \left( 1 + \frac{m_t}{m_e} \right) \operatorname{erf} \left( \frac{v_t}{\sqrt{2} v_{te}} \right) + Z_i \left( 1 + \frac{m_t}{m_i} \right) \operatorname{erf} \left( \frac{v_t}{\sqrt{2} v_{ti}} \right) \right] \right\}$$

and where  $m_t$ ,  $m_i$ , and  $m_e$  are the masses of the test particle, a plasma ion, and a plasma electron; where  $Z_t$  and  $Z_i$  are the ionization levels of the test particle and a plasma ion; where  $v_{te}$  and  $v_{ti}$  are the electron and ion thermal speeds; and where the Coulomb logarithm is

$$\log(\Lambda) \approx \log \left( \frac{3 (k_B T_e)^{3/2}}{2 \pi^{1/2} n_e^{1/2} Z_t e^3} \right) \cdot \quad (D-4)$$

From the slowing-down time, a slowing-down distance may be estimated by

$$R_s = v_t \tau_s ,$$

and from the rate of slowing, a stopping power of the test particle may be obtained,

$$\frac{dE}{dx} = m_t \frac{dv_t}{dt} ,$$

that yields (numerically) a range

$$R = \int_{E_0}^{E_f} \left( \frac{\partial E}{\partial x} \right)^{-1} dE ,$$

where  $E_0 = mv_0^2/2$  and  $E_f = mv_f^2/2$ , the final velocity  $v_f$  being  $v_0/e$ . For fifth-ionized gold traveling through a plasma with number density  $n_e = 3.41 \times 10^{15} \text{ cm}^{-3}$  (corresponding to 100% ionized air at a pressure  $P = 0.1$  torr) and temperatures  $T_e = 1.0$  eV and  $T_i = 0.2$  eV, the stopping power  $\partial E/\partial x$ , the slowing-down distance  $R_s$ , and the range  $R$  appear in Figs. D-1, D-2, and D-3 respectively. An example of interest is a gold ion with a velocity of  $2 \times 10^8$  cm/s; the results are

$$\frac{\partial v_t}{\partial t} = -1.89 \times 10^{13} \frac{\text{cm}}{\text{s}^2}$$

$$\frac{dE}{dx} = 3.88 \frac{\text{keV}}{\text{cm}}$$

$$t_s = 1.06 \times 10^{-5} \text{ s}$$

$$R_s = 2.21 \times 10^3 \text{ cm}$$

$$R = 531 \text{ cm} .$$

Note that if the velocities are preserved in the laser simulation, then the temperatures  $T$  and ionization levels  $Z$  are also preserved and therefore the slowing-down distance  $R_s$  and range  $R$  are proportional only to  $n_e^{-1}$  (neglecting the Coulomb logarithm with its very weak density dependence) and thus scale as distances and are preserved in the simulation. Note also that the slowing-down distance is a very strong function of velocity, the effective range of an ion traversing the plasma being approximately proportional to  $v^4$ .

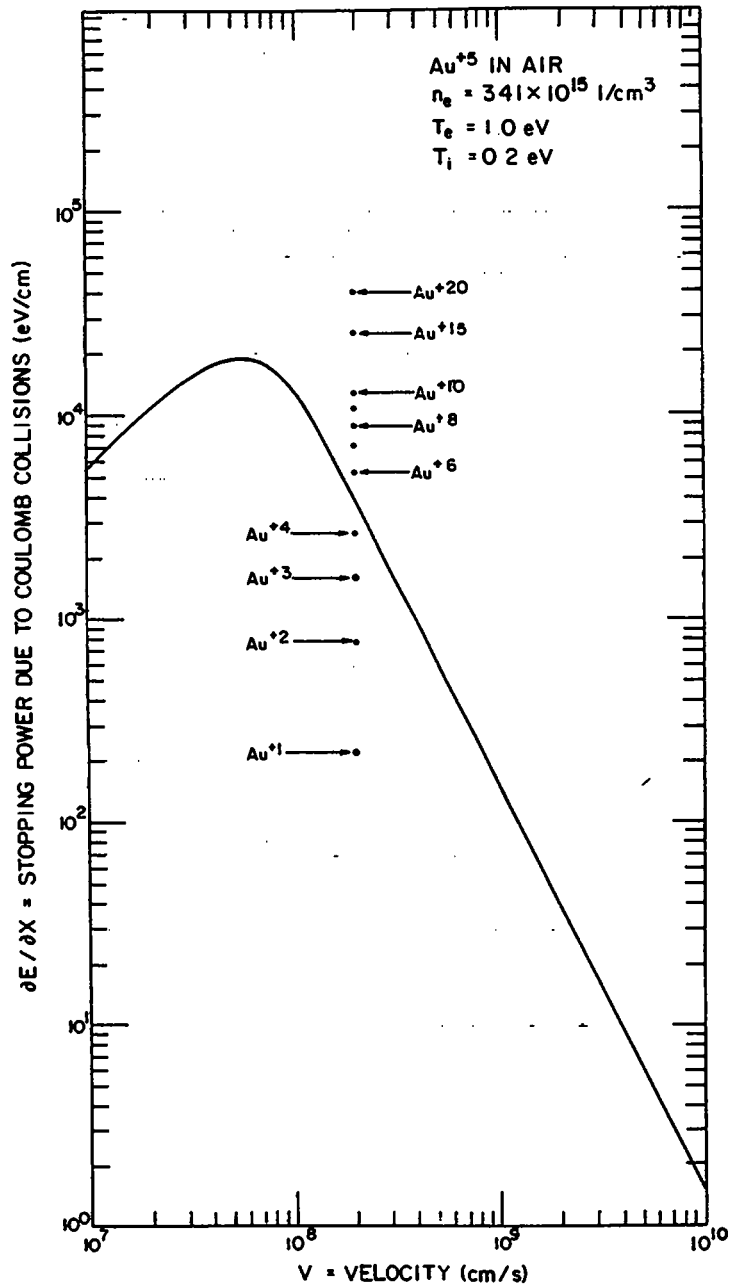


Fig. D-1. The stopping-power  $dE/dx$  arising from multiple Coulomb collisions for a fifth-ionized gold particle traversing singly ionized air with a number density of  $3.41 \times 10^{15} \text{ cm}^{-3}$  and electron and ion temperatures of 1.0 eV and 0.2 eV.

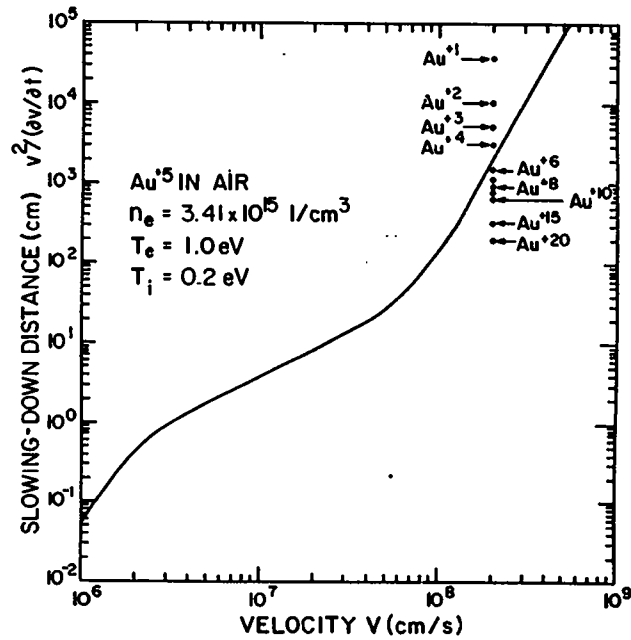


Fig. D-2. The slowing-down scale length  $R_s$  arising from multiple Coulomb collisions for a fifth-ionized gold particle traversing singly ionized air with a number density of  $3.41 \times 10^{15} \text{ cm}^{-3}$  and electron and ion temperatures of 1.0 eV and 0.2 eV.

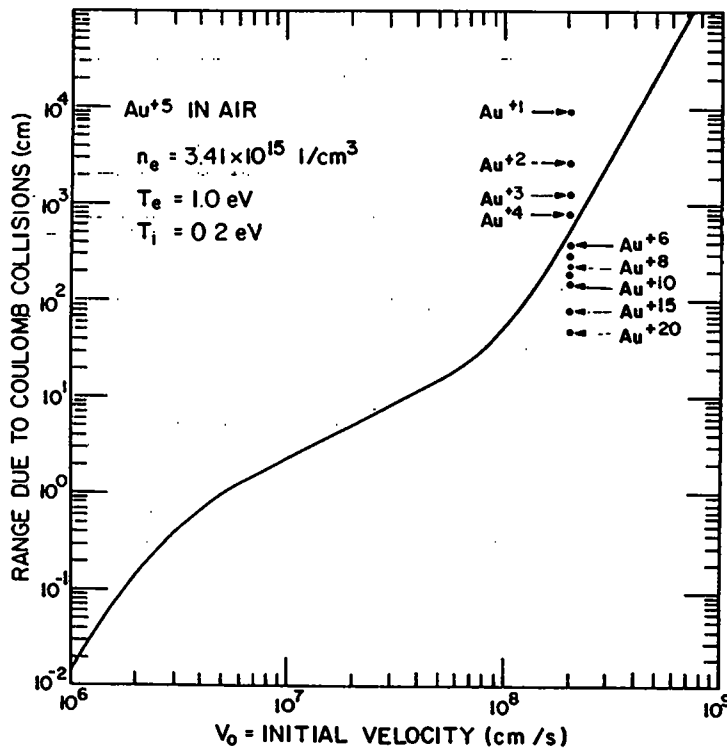


Fig. D-3. The range  $R$  arising from multiple Coulomb collisions of a fifth-ionized gold particle traversing singly ionized air with a number density of  $3.41 \times 10^{15} \text{ cm}^{-3}$  and electron and ion temperatures of 1.0 eV and 0.2 eV.

## CERENKOV EMISSION OF PLASMA WAVES

When a charged particle travels through a plasma at a velocity greater than the electron thermal velocity, the Debye shielding of the particle is both incomplete and asymmetric. This asymmetric cloud of charge exerts a force that leads to a slowing down of the particle, the energy lost by the particle being radiated away in longitudinal plasma oscillations excited by long-range Coulomb interactions between the incompletely shielded particle and the plasma electrons. The radiation of these collective modes is substantial only for particle velocities  $v$  greater than the electron thermal velocity and the waves radiated have frequencies  $\omega$  greater than the electron plasma frequency  $\omega_{pe}$ , with  $\omega \rightarrow \omega_{pe}$  as  $v \rightarrow \infty$ . Because of coherence effects, the wave vectors are associated with a Mach cone as are the vectors of the electromagnetic waves associated with the Cerenkov radiation by relativistic particles traveling through dielectrics (Ref. 9). Two estimates for the energy loss of a test particle with charge  $Ze$  traveling with velocity  $v_t$  through a plasma with an electron number density of  $n_e$  and electron temperature of  $T_e$  are

$$\frac{dE}{dx} = - 229 Z_{\xi}^2 \frac{n_e}{v_t^2} \log\left(1 + 3.80 \times 10^{-16} \frac{v_t^2}{T_e}\right) \frac{eV}{cm} \quad (\text{Ref. 19})$$

$$\frac{dE}{dx} = - 457 Z_{\xi}^2 \frac{n_e}{v_t^2} \log\left(2.39 \times 10^{-8} \frac{v_t}{T_e^{1/2}}\right) \frac{eV}{cm}, \quad (\text{Ref. 20})$$

( $n_e$  in units of  $\text{cm}^{-3}$ ,  $v_t$  in units of  $\text{cm/s}$ , and  $T_e$  in units of  $\text{eV}$ ). From the stopping power  $dE/dx$  a range may be obtained; using the stopping power of Ref. (20) above

$$R = 1.38 \times 10^{18} \text{ cm} \frac{T_e^2}{Z_{\xi}^2 n_e} \left[ \text{li}\left(\left\{\frac{2.39 \times 10^{-8} v_0}{T_e^{1/2}}\right\}^4\right) - \text{li}\left(\left\{\frac{8.79 \times 10^{-9} v_0}{T_e^{1/2}}\right\}^4\right) \right]$$

(same units as above), where  $\text{li}(x)$  is the logarithm-integral of  $x$ . Again, for

fifth-ionized gold traveling through a plasma with  $n_e = 3.41 \times 10^{15} \text{ cm}^{-3}$  and  $T_e = 1 \text{ eV}$ , these two relations give estimates for the energy loss of one particle to the Cerenkov emission of longitudinal plasma waves of

$$\frac{dE}{dx} = - 1.36 \frac{\text{keV}}{\text{cm}} \quad (\text{Ref. 19})$$

$$\frac{dE}{dx} = - 1.52 \frac{\text{keV}}{\text{cm}} \quad (\text{Ref. 20})$$

and a range of

$$R = 1.57 \times 10^3 \text{ cm} \quad (\text{Ref. 20})$$

Note that for velocity-preserving simulations  $dE/dx \propto n$  and  $R \propto n^{-1/2}$ , hence the collisionality of the simulation with respect to Cerenkov plasma processes is preserved. Note also that since  $dE/dx \propto v^{-2}$  and  $R \propto v^4$ , the collisionality with respect to Cerenkov plasma processes increases drastically as the velocity decreases.

#### COMPARISON

The relative stopping powers for the three processes, atomic and nuclear collisions, Coulomb collisions, and Cerenkov emission may be compared for fifth-ionized gold traveling at  $2 \times 10^8 \text{ cm/s}$  through 0.1 torr of 100% ionized air:

$$\frac{\partial E}{\partial x} = - 1.19 \frac{\text{keV}}{\text{cm}} \quad \text{atomic collisions}$$

$$\frac{\partial E}{\partial x} = - 3.88 \frac{\text{keV}}{\text{cm}} \quad \text{Coulomb collisions}$$

$$\frac{\partial E}{\partial x} = - 1.36 \text{ to } 1.52 \frac{\text{keV}}{\text{cm}} \quad \text{Cerenkov emission}$$

and

$$\frac{\partial E}{\partial x} \propto v^{0.962} \quad \text{atomic collisions}$$

$$\frac{\partial E}{\partial x} \propto v^{-2} \quad \text{Coulomb collisions}$$

$$\frac{\partial E}{\partial x} \propto v^{-2} \quad \text{Cerenkov emission} \quad ,$$

or,

$$R \propto v^{1.038} \quad \text{atomic collisions}$$

$$R \propto v^4 \quad \text{Coulomb collisions}$$

$$R \propto v^4 \quad \text{Cerenkov emission} \quad .$$

For this example of fifth-ionized gold at  $2 \times 10^8$  cm/s, all three processes contribute about equally, but for slower velocities the slowing down by Coulomb collisions and by Cerenkov emission will drastically dominate this slowing by atomic and nuclear collisions.

#### ALUMINUM DEBRIS

Using a 1-mm-diam aluminum-coated target, aluminum debris ions with velocities of  $\sim 2 \times 10^8$  cm/s are anticipated in the Helios experiment. Some pertinent collisional parameters for  $2 \times 10^8$  cm/s aluminum traveling through 0.1 torr of 100% ionized air are

$$\frac{dE}{dx} = 5.13 \times 10^2 \frac{eV}{cm} \quad \text{atomic and nuclear collisions} \quad (\text{Ref. 14})$$

$$R = 1100 \text{ cm} \quad \text{atomic and nuclear collisions} \quad (\text{Ref. 14})$$

$$R = 108 \text{ cm} \quad \text{multiple Coulomb scattering (fourth-ionized)}$$

$$R = 2450 \text{ cm} \quad \text{Cerenkov emission (fourth-ionized)} \quad .$$

Figure 18 compares the multiple Coulomb scattering ranges for variously charged aluminum ions with the range, which are due to atomic and nuclear processes. The value of  $dE/dx$ , when compared to the value of  $dE/dx$  for protons of the same velocity, yields the effective charge state of the aluminum as

$$Z_{\text{eff}} = 3.48$$

#### REFERENCES

1. C. L. Longmire, "Notes on Debris-Air-Magnetic Interaction," Rand Corporation memorandum RM-3386-PR (1963).
2. J. F. Velecky, J. W. Chamberlain, J. M. Cornwall, D. A. Hammer, and F. W. Perkins, "Irregularities in Ionospheric Plasma Clouds: Their Evolution and Effect on Radio Communication," JASON Technical Report JSR-80-15 (1980).
3. C. Longmire, M. Alme, R. Kilb, and L. Wright, "Scaling of Debris-Air Coupling," Mission Research Corporation report AMRC-R-338 (1981).
4. M. Cornwall, S. Flatté, D. Hammer, and J. Vesecky, "Studies on the Effect of Striations on Radio Communications," JASON Technical Report JSR-81-31 (1981).
5. COSPAR Working Group IV, COSPAR International Reference Atmosphere 1965 (North-Holland Publishing Company, Amsterdam, 1965).
6. R. L. Carlson, J. P. Carpenter, D. E. Casperson, R. B. Gibson, R. P. Godwin, R. F. Haglund, Jr., J. A. Hanlon, E. L. Jolly, and T. F. Stratton, "Helios: A 17 TW Carbon Dioxide Laser-Fusion Facility," IEEE J. Quantum Electron. QE-17, 1662 (1981).
7. T. H. Tan, G. H. McCall, and A. H. Williams, "Determination of Laser Intensity and Hot Electron Temperature from Fastest Ion Velocity Measurement on Laser Produced Plasma" Los Alamos National Laboratory document LA-UR-82-1488, submitted to Phys. Fluids (1982).
8. D. Forslund and J. Brackbill, "Magnetic-Field-Induced Surface Transport on Laser-Irradiated Foils," Phys. Rev. Lett. 48, 1614 (1982).
9. P. Marmier and E. Sheldon, Physics of Nuclei and Particles, Vol. I, Secs. 4.9 and 4.10 (Academic Press, New York, 1969).
10. T. P. Hughes, Plasmas and Laser Light (John Wiley and Sons, New York, 1975).
11. J. Zinn and C. D. Sutherland, "Structure and Luminosity of Radiative Thermal Waves in Air," Los Alamos National Laboratory document LA-UR-81-1893 (1981).

12. D. H. Holland, A. M. Kaufman, and A. A. O'Dell, "The Transport and Deposition of Ionizing Radiation," in Physics of High-Altitude Nuclear Burst Effects, Mission Research Corporation report DNA-4501F (1977).
13. J. Lindhard and M. Scharff, "Energy Dissipation by Ions in the keV Region," Phys. Rev. 124, 128 (1961).
14. L. C. Northcliffe and R. F. Schilling, "Range and Stopping-Power for Heavy Ions," Nuclear Data Tables, A7, 233 (1970).
15. J. T. Tate and P. T. Smith, "The Efficiencies of Ionization and Ionization Potentials of Various Gases Under Electron Impact," Phys. Rev. 39, 270 (1932).
16. A. Omholt, "Particle Precipitation: Ionization and Excitation," in Cosmical Geophysics, A. Egeland, O. Holter, and A. Omholt, Eds., (Scandinavian University Books, Oslo, Norway, 1973).
17. S. K. Allison, "Experimental Results on Charge-Changing Collisions of Hydrogen and Helium Atoms and Ions at Kinetic Energies Above 0.2 keV," Revs. Modern Phys. 30, 1137 (1958).
18. N. A. Krall and A. W. Trivelpiece, Principles of Plasma Physics, Sec. 6.4 (McGraw-Hill, New York, 1973).
19. D. Pines and D. Bohm, "A Collective Description of Electron Interactions: II. Collective vs Individual Particle Aspects of the Interactions," Phys. Rev. 85, 338 (1952).
20. N. Rostoker and M. N. Rosenbluth, "Test Particles in a Completely Ionized Plasma," Phys. Fluids 3, 1 (1960).

Printed in the United States of America  
Available from  
National Technical Information Service  
US Department of Commerce  
5285 Port Royal Road  
Springfield, VA 22161

Microfiche (A01)

Page Range	NTIS Price Code						
001-025	A02	151-175	A08	301-325	A14	451-475	A20
026-050	A03	176-200	A09	326-350	A15	476-500	A21
051-075	A04	201-225	A10	351-375	A16	501-525	A22
076-100	A05	226-250	A11	376-400	A17	526-550	A23
101-125	A06	251-275	A12	401-425	A18	551-575	A24
126-150	A07	276-300	A13	426-450	A19	576-600	A25
						601-up*	A99

\*Contact NTIS for a price quote.

Los Alamos